

AN ABSTRACT OF THE DISSERTATION OF

Malachi D. Bunn for the degree of Doctor of Philosophy in Chemical Engineering
presented on August 14, 2015.

Title: Aging and Performance Evaluation of Marine Antifouling Coatings.

Abstract approved: _____

Alexandre F. T. Yokochi

Marine biofouling is a major problem in many industries. Shipping has been afflicted with reduced vessel speed and hindered maneuverability due to organisms attaching since the dawn of sailing. To date, the primary method developed to prevent fouling is the application of biocide laden coatings with various release mechanisms. Mass loss and coating degradation are the fundamental operational principles by which these coatings operate, which in turn limit their operational lifetime, requiring hull dry-docking to recoat for continued fouling prevention. With the advent of marine hydrokinetic technology as a possible contributor to the renewable energy landscape, there is a real need for longer life antifouling systems, since frequent dry-docking of these hulls is undesirable. Electrochemical antifouling systems with very long operational lifetimes may fulfill this need. These systems utilize electricity and the chloride found abundantly in seawater to sterilize surfaces, which replaces coating degradation as the operating principle of these systems.

In support of system development and future design engineering, contributing to the body of knowledge in this new technology, test methods have been developed to determine threshold conditions under which fouling is effectively prevented in local conditions, accelerated aging tests of the electrochemical performance of the coatings were measured, and the surface concentration of electrochemically generated oxidizer species are determined. Using simple potentiostatic control circuits designed specifically for these experiments, it was determined that a threshold applied potential of 1.12 V vs.

Ag|AgCl(seawater) reference electrodes is required for effective biofouling prevention. The electrochemical reaction kinetics have been modeled and verified in purpose built electrochemical reactors, yielding parameters measured as a function of galvanostatic aging. The vast majority of the experiments showed no statistically significant change in the operational parameters for the electrochemically active coatings, indicating that this biofouling prevention technology has the potential for very long operational lifetimes. Determining the effectiveness of oxidizer production in chloride bearing systems (3.5% w/v NaCl and synthetic seawater) shows that the trace bromide present in seawater does slightly enhance the system performance, and that the electrochemical work carried out in 3.5% NaCl therefore yields a lower bound estimate of the energy consumption of the process. Further, from the combined use of the flow cell and modelling we were able to determine that at the 1.12V threshold voltage determined, the concentration of oxidizer species in the transition layer at the surface of the chloride oxidation reactor is 1.5ppm, which is comparable with the ca. 0.5 – 1.5 ppm range of concentrations required to effectively sterilize swimming pool water.

©Copyright by Malachi D. Bunn

August 14, 2015

All Rights Reserved

Aging and Performance Evaluation of Marine Antifouling Coatings

By

Malachi D. Bunn

A DISSERTATION

submitted to

Oregon State University

in partial fulfillment of
the requirements for the
degree of

Doctor of Philosophy

Presented August 14, 2015

Commencement June 2016

Doctor of Philosophy dissertation of Malachi D. Bunn presented on August 14, 2015.

APPROVED:

Major Professor, representing Chemical Engineering

Head of the School of Chemical, Biological, & Environmental Engineering

Dean of the Graduate School

I understand that my dissertation will become part of the permanent collection of Oregon State University libraries. My signature below authorizes release of my dissertation to any reader upon request.

Malachi D. Bunn, Author

ACKNOWLEDGEMENTS

I would like to thank my family and friends for being supportive through the long hours that have been devoted to producing this work, and understanding my vacancy. I would also like to thank my advisor, Alex Yokochi for his guidance throughout my graduate studies, and my lab mates, past and present, for their contributions to my growth both in asking and answering important questions. A special thank you goes out to Peter Kreider and Matthew Ryder for helping me maintain my sanity during the final months of experiments and writing.

I also gratefully acknowledge support for this work from the US Department of Energy (Award Number DE-FG36-08GO18179) for the Northwest National Marine Renewable Energy Center (NNMREC), and the State of Oregon Capital Funding Program.

DISCLAIMER

This report was prepared as an account of work sponsored by an agency of the United States Government. Neither the United States Government nor any agency thereof, nor any of their employees, makes any warranty, expressed or implied, or assumes any legal liability or responsibility for the accuracy, completeness, or usefulness of any information, apparatus, product, or process disclosed, or represents that its use would not infringe privately owned rights. Reference herein to any specific commercial product, process, or service by trade name, trademark, manufacturer, or otherwise does not necessarily constitute or imply its endorsement, recommendation, or favoring by the United States Government or any agency thereof. Their views and opinions of the authors expressed herein do not necessarily state or reflect those of the United States Government or any agency thereof.

TABLE OF CONTENTS

	<u>Page</u>
1. Introduction.....	1
1.1 Overview.....	1
1.2 Research Goals and Objectives	3
1.3 Contribution to Science.....	3
2. Background.....	5
2.1 The Marine Hydrokinetic Resource.....	5
2.2 The Problem of Marine Fouling Organisms.....	6
2.3 Commercial Antifouling Technology Overview.....	7
2.4 Testing of Current Antifouling Coatings.....	8
2.5 Directions of Modern Antifouling Research.....	9
2.6 Electrochemical Antifouling Technology.....	10
2.7 Chlorine Electrochemistry	11
2.8 Electrochemistry Overview	12
2.9 Microchannel Reactor Design	18
2.10 Graphite Composite Electrodes and Conduction in Thin Composite Films	19
2.11 Graphite Electrode Degradation	21
2.12 The 1-D Terminal Effect Model	21
3. Materials and Methods	25
3.1 Graphite Paints.....	25
3.2 Sheet Resistance Measurement.....	26
3.3 Electrolytes	27
3.4 Area Determination.....	28
3.5 Voltage Profile Experiments.....	28
3.6 Analytical Solution of Terminal Effect Model and Voltage Profile Analysis	31
3.7 Discrete Voltage Profiling.....	33
3.8 Non-Graphitic Materials.....	35

TABLE OF CONTENTS (Continued)

	<u>Page</u>
3.9 Electrochemical Reactor Production.....	36
3.10 Electrochemical Reactor Operation	39
3.11 Aging Experiments.....	40
4. Modeling and Parameter Fitting	46
4.1 The Model.....	46
4.2 Reactor Model Characteristics	50
5. Results and Discussion.....	53
5.1 Paint Development.....	53
5.2 Terminal Effect Model.....	55
5.3 Parallel Potentiostatic Flow Cell.....	56
5.4 Non-Graphitic Materials.....	57
5.5 Electrochemical Reactor Results	58
5.6 Degradation Studies	68
6. Conclusion	81
6.1 Future Work	82
7. Bibliography.....	84
Appendices	89
Appendix A Butler-Volmer Fitting Routine.....	90
Appendix B Constants Used in Model Parameter Fitting.....	92

LIST OF FIGURES

<u>Figure</u>	<u>Page</u>
Figure 2.2.1. Progression of fouling on gel-coat type coating in Yaquina Bay, OR.	6
Figure 2.8.1. Physical interpretation of charge transfer coefficient.....	14
Figure 2.8.2. An ideal Butler-Volmer plot with equilibrium potential of 0.7V	15
Figure 2.10.1 Resistivity of composite material as function of conductive filler volume fraction.....	19
Figure 2.10.2 Diagram of a 4 point probe.....	20
Figure 2.11.1 Resistive electrode with insulating backing.....	22
Figure 3.1.1 Graphite paint samples applied to insulated fiberglass backing.....	25
Figure 3.2.1 The spring loaded contact with uniformly spaced probes provided repeatable contacting for 4PP measurements, highlighted by the red dashed rectangle.	26
Figure 3.3.1 with permission from previous work by Matthew Delaney[1].	29
Figure 3.3.2 Ocean Sentinel voltage profile experiment.....	30
Figure 3.3.3 Simple in-house built potentiostat circuit diagram.....	30
Figure 3.7.1 Parallel channel flow reactor design.	33
Figure 3.7.1 Methylene blue injection into feed results in fairly even distribution.....	35
Figure 3.8.1 Test of alternative materials for electrochemical antifouling performance prior to deployment.....	36
Figure 3.9.1 Taig Micro-CNC mill used to machine reactor blanks from polycarbonate bar stock.	37
Figure 3.9.2 CAD rendering of reactor halves after first stage of machining. Curves in the paint wells are fillets due to the 3/16in end mill used	37
Figure 3.9.2 Photograph of a finished reactor half.....	38

LIST OF FIGURES (Continued)

<u>Figure</u>	<u>Page</u>
Figure 3.11.1 Galvanostatic aging apparatus.....	40
Figure 3.11.2 Bob's Electrochemical Cell used for electrochemical measurements.	41
Figure 3.11.3 Graphite paint electrodes prepared on graphite rods.	42
Figure 3.11.4 Graphite paint coated PVC tube electrodes.....	43
Figure 4.1 Diagram of reactor being modeled.	46
Figure 4.1.1 Comparison of model with experimental results and naïve Tafel kinetic model.	50
Figure 4.2.1 Concentration of hypochlorite throughout reactor model with device flowrate of 4.0L/min.	51
Figure 4.2.2 Close-up view of electrode surface at reactor outlet.....	51
Figure 5.1.1 Sheet resistance as a function of graphite composition.	53
Figure 5.1.2 CV scan of graphite paint electrode on PVC tube base in potassium ferrocyanide electrolyte described in Section 3.3.....	54
Figure 5.1.3 Dependence of CV peak current on scan rate in potassium ferrocyanide electrolyte.	54
Figure 5.2.1 Potential supplied to working electrode, with reference to Ag AgCl wire in seawater.	55
Figure 5.3.1 Device upon retrieval after 20 days in the field.	56
Figure 5.3.2 Flow device dried with cover removed. Several channels have clear algae fouling, while all show significant copper oxide development.	56
Figure 5.3.3. Current data logger for channel 2.	57
Figure 5.4.1 TiN and ITO coatings recovered after six days in filtered seawater tank at Hatfield Marine Science Center.....	58

LIST OF FIGURES (Continued)

<u>Figure</u>	<u>Page</u>
Figure 5.5.1 Current-voltage plot from electrochemical reactor fed with non-reactive supporting electrolyte.	59
Figure 5.5.2 Current-voltage plot from electrochemical reactor fed with non-reactive KNO ₃ supporting electrolyte, with and without blue 1 dye	60
Figure 5.5.3. Absorption signal clearly indicates bleaching activity. Reaction could either be direct oxidation of the dye or bleaching due to hydrogen peroxide generation	60
Figure 5.5.4 Current draw difference between chloride and KNO ₃ electrolytes with blue 1 dye.	61
Figure 5.5.5 Chloride electrolyte current and absorbance comparison at flow rate of 0.9mL/minute.	62
Figure 5.5.6 Chloride electrolyte current and absorbance comparison at flow rate of 1.8mL/minute.	62
Figure 5.5.7 Chloride electrolyte current and absorbance comparison at flow rate of 3.4mL/minute.	63
Figure 5.5.8 Current dependence on voltage, variation with flow rate in chloride electrolyte.	63
Figure 5.5.9 Absorbance signal as function of voltage at four flow rates.....	64
Figure 5.5.10 Current comparison of chloride and bromide electrolytes at 1.6mL/min flow rate.....	65
Figure 5.5.11 Absorbance comparison of chloride vs bromide electrolytes.....	65
Figure 5.5.12 Current and absorbance as functions of voltage for bromide electrolyte.	66
Figure 5.5.13 Absorbance-voltage curves for chloride electrolyte and synthetic seawater	67
Figure 5.5.14 Current-voltage curves for chloride electrolyte and synthetic seawater...	67

LIST OF FIGURES (Continued)

<u>Figure</u>	<u>Page</u>
Figure 5.6.1 Observed changes in exchange current density as a function of cumulative current experienced by three independent electrodes	68
Figure 5.6.2 Exchange current density normalized to initial values.	69
Figure 5.6.3 Charge transfer coefficient variation with aging.	69
Figure 5.6.4 Charge transfer coefficient normalized to initial values.	70
Figure 5.6.5 Exchange current density as function of aging.....	71
Figure 5.6.6. Reduction charge transfer coefficient as function of aging for graphite filled polyurethane paints on graphite rods in chloride electrolyte.....	72
Figure 5.6.7 Exchange current density as function of aging for second set of 3 electrodes	72
Figure 5.6.8 Charge transfer coefficient as function of aging for second set of three electrodes, Tafel scans taken in purged electrolyte.	73
Figure 5.6.9 Graphite paint on graphite rod samples after aging in chloride electrolyte.	74
Figure 5.6.10 Exchange current density of graphite paint on PVC rods measured with pulsed voltammetry method as function of galvanostatic aging in chloride electrolyte. 74	
Figure 5.6.11 Normalized exchange current density with aging in chloride electrolyte..	75
Figure 5.6.12 Charge transfer coefficient with aging in chloride electrolyte.....	76
Figure 5.6.13 Charge transfer coefficient for oxidation reaction on graphite paint electrode, comparison of aged and unaged electrodes.....	76
Figure 5.6.14 Comparison of reduction charge transfer coefficient with exposure time in chloride electrolyte.....	77
Figure 5.6.15 Comparison of exchange current density with exposure time in chloride electrolyte.....	77
Figure 5.6.16 Aged and control electrode charge transfer coefficient	78

LIST OF FIGURES (Continued)

<u>Figure</u>	<u>Page</u>
Figure 5.6.17 Aged and control electrode exchange current density	78
Figure 5.6.18 Charge transfer coefficient as a function of galvanostatic aging.	79
Figure 5.6.19 Exchange current density as a function of galvanostatic aging.	79
Figure 5.6.20 Normalized exchange current density as a function of galvanostatic aging.	80
Figure 5.6.21 Electrode after anodic aging at $211\mu\text{A}/\text{cm}^2$ in bromide electrolyte, showing some clear physical change	80

List of Tables

<u>Table</u>	<u>Page</u>
Table 3.7 Table of applied potentials in parallel potentiostatic flow cell experiment.....	35
Table 3.9 Summary of aging experiment conditions	44

1. Introduction

1.1 Overview

Wave energy conversion is a promising field for renewable energy development. The wave energy resource is vast and available to most major population centers [2]. One challenge facing the development of wave energy buoys is the age old problem of preventing colonization of marine organisms such as algae, muscles, barnacles, etc. on exposed surfaces. Of concern in the particular case of wave energy devices is clogging of gaps between moving parts leading to seizure and device failure.

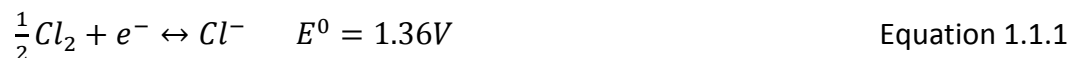
This problem has been previously approached with a focus on shipping, where added drag reduces speed and maneuverability, as well as increases fuel consumption. According to a study by the United States Office of Naval Research, uncontrolled fouling may increase fuel consumption by as much as 40% in ocean going vessels [3], while another study found that drag may increase by as much as 86% for heavily fouled ships[4]. Barnacles and large algal species obviously add greater drag, however even biofilms may add significant drag to a ship's hull [5]. As the shipping industry accounts for more than 2% of global greenhouse gas emissions [6], the economic and environmental implications of uncontrolled fouling are obvious and substantial.

Historical attempts at preventing fouling vary widely including the use of oils/tar, sacrificial second hulls, lead and copper plating, among others [7]. Probably the most successful method for preventing fouling to date is the use of self-polishing organic-tin resins which were introduced in the 1970s [8]. Organic-tin paints were very successful until the environmental harm of their use became apparent [9, 10]. Use of these paints is now prohibited almost universally, in all 171 member states and 3 associate member states of the International Maritime Organization [10, 11].

Since the ban on tin-containing self-polishing resins there has been a push to find new high performance coatings which will not be subject of a similar ban. Various organic and inorganic biocides have been tested in self-polishing resins achieving

acceptable performance, but whenever toxic chemicals are involved, the possibility of a ban looms [12, 13]. Several less-toxic and non-toxic schemes have also been proposed to prevent fouling on marine structures: so called natural chemical biocides [9, 14-16], surface chemistry modification [17, 18], micro and nano scale surface structures [19, 20], immobilized or very low release biocides [21], foul-release or “super-slick” coatings [22-26], and electrochemical methods [27-29] are some of the major areas of research focus. Electrochemical methods using conductive paint films appear to be a good option for large scale use due to ease of application and efficacy, without requiring high water velocity over the surface as in super-slick technologies.

Electrochemical activation of chloride ions present in water produces chlorine gas, which rapidly disproportionates forming hypochlorite in basic conditions as in Equations 1.1.1 and 1.1.2 [30].



This generation of bleach has been shown to be effective in preventing fouling on industrial process water inlets, netting material exposed to seawater, and oral implants used in dentistry [27-29, 31]. It has also been proposed as a means of disinfecting water for human consumption [32, 33]. Electrochemical protection of large or complex surfaces may thus be achieved via application of conductive coatings, allowing electrical potential to be applied to the surface. Previous work has used graphite powder in polyurethane resin (PU) to create a conductive paint film [1, 27, 34]. Electrochemical potentials used to achieve antifouling performance in literature are in the range of +0.60V to +1.2V v standard calomel electrode (SCE)[27, 35]. The potential required to effectively prevent fouling is expected to be a function of the oxidized chlorine species concentration and of the fouling species present.

Characterization of electrode activity, and in particular activity as a function of degradation over time, is necessary to predict electrode performance into the future, allowing industrialization of the technology. Initial characterization of electrochemical properties of the graphite/PU electrode was conducted by Matthew Delaney at OSU[1]. The purpose of the proposed research is to conduct further studies characterizing degradation and hypochlorite concentration profile model parameters.

1.2 Research Goals and Objectives

The overall motivation for this research was to determine whether electrochemical methods utilizing conductive paints may inexpensively and effectively prevent fouling organisms from colonizing marine surfaces while causing minimal environmental impact. In support of answering this question the following objectives were met:

1. Graphite degradation model for graphite filled polyurethane electrodes under anodic conditions in seawater was developed and validated.
2. A model predicting the Br_2 and ClO^- concentrations at the surface of graphite filled polyurethane electrodes in seawater was developed.
3. An electrochemical reactor suitable for testing the model was designed and built.
4. Experimental results were used to fit model parameters.
5. The model developed in (2) was applied to determine the minimum concentration of hypochlorite required to prevent biofouling at the test berth established by the Northwest National Marine Renewable Energy Center off the coast of Newport, OR.

1.3 Contribution to Science

This work contributes to science in several ways: the electrode kinetics for chloride oxidation on graphite paint electrodes are previously unstudied, as is the reaction selectivity of such an electrode used in seawater, and the degradation studies

contribute new knowledge in the field of graphite degradation. Results of this work have been presented at professional meetings including IEEE SusTech 2014, Marine Energy Technology Symposium 2014, AIChE Spring Meeting 2014, ACS National Meeting and Exposition 2013, ACS Northwest Regional Meeting 2012, and AIChE Annual Meeting 2012. Peer reviewed journal articles have been published in *Shore and Beach*[36] are under preparation for submission to *Biofouling* and *Journal of the Electrochemical Society*.

2. Background

2.1 The Marine Hydrokinetic Resource

It is well known and accepted that the side effects of most current electrical energy generation technologies are climate change and pollution, both of which are detrimental to human well-being. Additionally, conventional energy resources such as crude oil are concentrated in geopolitically fragile or unstable regions. Technologies for renewable energy harvest are desirable to minimize anthropogenic impacts on the environment, as well as to ensure sufficient, stable supplies of energy worldwide. Wind, solar, geothermal, and hydropower are the major renewable energy technologies, each with its own advantages and disadvantages. Not all resources are suitable in all locations, and implementation of diverse systems adds robustness to the overall system as well as reducing the magnitude of environmental impacts from any one technology. Marine hydrokinetic energy (MHK) is a subset of hydropower, harvesting energy from tidal surge or waves, rather than the more traditional river dam. The wave energy resource available along the outer continental shelf of the United States was estimated to be 2,640TW-h/year [2]. The same study estimated the technically recoverable energy of that available was 1,170TW-h/year. Wave energy alone will not meet the nation's demand for power, which was 4,066TW-h in 2013 [37], but development of this resource will be an important piece of the renewable energy puzzle.

As a relatively immature field, MHK energy has few accepted industry standards, and no widely accepted notions of what the most efficient systems will be. System designs range from clam-shell flappers on the seafloor to overtopping dams; from subsurface turbines to a wide array of buoys. Each concept leads to a highly engineered system, designed to be deployed in a rough environment without easy access for maintenance. Biofouling will pose as much of a threat to device survivability as the other likely culprits: corrosion, ship-strikes, and storm damage. To reduce the cost of implementation and therefore advance the MHK field, adequate protection from biofouling must be provided.

2.2 The Problem of Marine Fouling Organisms

Marine biofouling is an ancient problem which has yet to be satisfactorily resolved. Biofouling is the general term for unwanted accumulation of biomass on man-made structures. While biofouling is also an issue in freshwater environments and for medical devices, the focus of this work is preventing fouling in the marine environment. For the purpose of this work, fouling will be used to denote biofouling, as inorganic fouling such as heat exchanger scale is not considered. Fouling begins rapidly upon exposure to seawater. Organic molecules begin adsorbing immediately, paving the way for bacterial biofilms which form in the first 24 hours, algal colonization in the first week, and invertebrate colonization within 2-3 weeks [7]. Figure 2.2.1 demonstrates the stages of fouling on a gel-coat sample plate left in Yaquina Bay, OR.

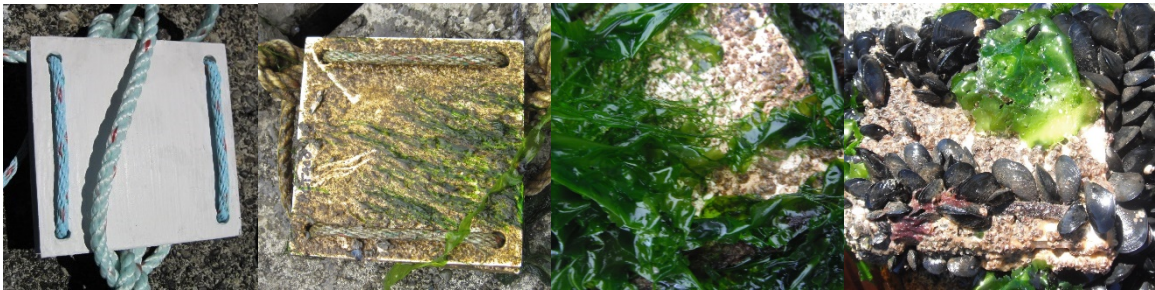


Figure 2.2.1. Progression of fouling on gel-coat type coating in Yaquina Bay, OR. From Left to right: clean surface, 1 month of exposure showing bacterial slime and algal growth, 2 months of exposure showing large algal species attachment, and 12 months of exposure showing significant barnacle and mussel attachment.

Biofouling is generally classified as hard fouling such as barnacles and mussels which are relatively easy to control, yet adhere strongly, and soft fouling such as bacterial films and various algae species which are easier to remove, however harder to prevent [38]. According to a study by the United States Office of Naval Research, uncontrolled fouling may increase fuel consumption by as much as 40% in ocean going vessels [3], while another study found that drag may increase by as much as 86% for heavily fouled ships [4]. Barnacles and large algal species obviously add greater drag, however even biofilms may add significant drag to a ship's hull[5]. As the shipping industry accounts for more than 2% of global greenhouse gas emissions[6], the

economic and environmental implications of uncontrolled fouling are obvious and substantial.

Increased drag force due to fouling is also of great concern for MHK devices, many of which are tuned to optimize energy capture from the spectral range of ocean waves. Added mass and drag will damp the device motions, reducing device efficiency. The harm may be much greater than lost efficiency if fouling clogs pinch points and causes device failure. Any design utilizing a turbine will suffer from accumulation on the leading edge altering fluid dynamics. Depending on material choices, microbially induced corrosion[8] may be a concern. Water intake clogging [28] is also a significant issue that will impact overtopping designs. MHK devices differ from other marine equipment in that they are not designed to move about once deployed, and they are deployed potentially many miles off-shore in rough seas. This creates a situation in which dry dock service is not feasible, and long service interval protection from fouling is necessary.

2.3 Commercial Antifouling Technology Overview

Commercially available antifouling paints are predominantly copper based due to the efficacy of copper in preventing animal settlement. These are often augmented with additional organic herbicides to combat algae and biofilm growth. The most basic type of antifouling paint is the hard-coat type, in which the paint film is mechanically durable, such as an epoxy, and biocide leaches at a time dependent rate. Hard coat antifouling paints leach large excesses of biocide initially and deplete rapidly. Self-polishing paints are a more advanced technology. They utilize a hydrolysable matrix which breaks down and becomes water soluble over time. There are two major advantages of self-polishing antifouling paints: the mechanical breakdown of the film causes sloughing action, which removes fouling organisms which may attach, and the eroding matrix also allows for a steady release of biocide. The release rate of biocide from hard coat [39] and self-polishing films [40] have each been modeled successfully by previous researchers. Hard coat paints have short useful lives, while self-polishing paints have service intervals of up to 5 years [38].

Biocide-free antifouling paints are commercially available as well. These are predominantly slick-type coatings and non-biocidal self-polishing coatings. Slick coatings such as silicones and fluoropolymers seek to make adhesion more difficult for would-be fouling organisms, and to make removal of organisms which do successfully settle on the surface easier. Manufacturer claims for slick type coatings boast as long as 90 month service interval between dry docking [41]. A limitation of this type of coating is the requirement for water velocity sufficient to impede settlement and clean the surface, for example 8 knots as required by the aforementioned Hempasil X3 coating. Purely self-polishing paints utilize sloughing action to maintain a fresh surface. These coatings are available, though not as popular as other coating types.

2.4 Testing of Current Antifouling Coatings

Detailed mechanistic studies have been undertaken to support the ability of manufacturers to tailor make self-polishing antifouling paints based on expected environmental conditions [42]. The behavior of self-polishing biocide based antifouling paints is such that the biocide pigment rapidly diffuses out of the matrix until a depleted polymer region is established. Release is held steady because the biocide depletion front moves at the same rate as the polymer erosion front in a quasi-steady-state fashion [43]. Establishing this steady state condition may take as long as 80 days. Successful models of these paints assume a saturated pigment concentration at the pigment depletion front [40]. While many factors, such as pigment particle size, inert pigment loading, and binder hydrophobicity will impact the release rate, to test an established paint system, environmental variables to be mindful of are those which affect pigment solubility and/or rate of solution (pH, temperature, Cl^- concentration), those which impact binder hydrolysis rate (temperature, pH, NaCl concentration), and those which impact the physical erosion process (surface water speed, turbidity) [42]. How strongly these factors affect the leaching process will vary strongly with pigment and binder type.

Current practice for testing of self-polishing biocide release coatings involves rotating drum experiments, which measure release rates of biocide pigments under fixed flow and controlled environmental conditions. ASTM standards D6442-06 and D6903-07 specify standard means for determination of copper and organic biocide release rates from antifouling paints, respectively. While the ASTM standards do not yield accurate release rates for coatings in a particular environment, they provide convenient in-lab comparison of relative release rates. The drum method has been extended to measuring of ablation rate as well [44]. The major factor limiting test throughput is the time required to generate measurably significant erosion.

Non-biocidal, slick-type coatings are of great interest to minimize potential environmental impacts due to anti-fouling technology. Under stagnant conditions these coatings are seldom effective. Slick-coatings will rely on cleaning due to natural water motion, or possibly periodic cleaning by submersible remote operated vehicles. In either case, the adhesive strength of various organisms are critical performance parameters. In laboratory studies, adhesive strength tests are achieved using a force gauge to scrape off barnacle analogues perpendicular to the bond [24]. Slick type coatings utilize a variety of chemical compositions with a variety of weaknesses and breakdown mechanisms. As a result, a generalized aging mechanism is therefore unsuitable for this class of coatings. Performance qualification of these coatings will rely on comparison of fouling organism density in field trials and organism adhesion strength tests.

2.5 Directions of Modern Antifouling Research

Tributyl-tin self-polishing paints were the height of antifouling performance. Unfortunately the environmental impacts of organo-tin pollution were severe enough to warrant an all-out ban on their use imposed by the International Maritime Organization in the first decade of the millennium. Since the ban on tin containing antifoulants, there has been a push to develop comparable antifouling systems. While copper and various modern herbicides have been proven effective, there is still major concern about

potential environmental impacts of releasing biocidal components [13]. Consequently substantial research has been directed at developing non-biocidal coatings [45], coatings with biomimetic biocides [16], and other antifouling technologies [46-48].

Non-biocidal slick-type coatings are commercially available, however not very mature technologically. Recent research in support of foul release coatings has looked at fouling organism adhesive strength [25, 49], effects of polymer surface energy [50, 51], and effects of physical surface texturing [20, 52]. It is unlikely that slick type coatings will be sufficient for MHK demands, due to the need for water movement, durability issues, and complications with applying nano- and micro-textures to large surfaces. Other technologies such as sonic and electrochemical antifouling have been largely disregarded due to cost, corrosion concerns, and system complexity [10]. Due to the decreasing cost of electronics and advancement of polymer materials for hulls, the perceived shortcomings of electrochemical antifouling systems may be over-stated.

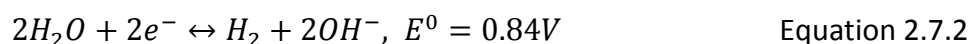
2.6 Electrochemical Antifouling Technology

Electrochemical antifouling technology utilizes electricity to generate a hostile environment for would-be fouling organisms at the protected surface. Research has shown that direct electron transport or even static charge alone may be sufficient to repel bacterial cells and therefore reduce fouling [27, 35], however the voltages used in many reports of antifouling performance are beyond the threshold for bromide and/or chloride oxidation [28, 31, 46, 53]. Given these sufficient potentials, chloride and bromide present in seawater will oxidize forming hypochlorous acid in equilibrium with hypochlorite and bromine, respectively. Either of these species are toxic at low doses and act as effective antifouling agents. While chloride oxidation has been heavily studied in the context of the chlor-alkali process, materials and conditions relevant for antifouling use remain largely unstudied. Most studies of electrochemical antifouling technology are basic proofs of concept [27, 38, 47, 54, 55]. The mechanism of action has been proposed to be generation of reactive oxygen species [46], direct electron transfer, charge repulsion[53], and chloride oxidation [1, 29, 32]. In reality all of these

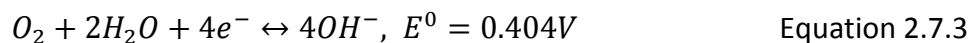
likely play a role, however it is clear that the kinetics of electrochemical reactions in seawater are not well characterized.

2.7 Chlorine Electrochemistry

The Chlor-Alkali process is a major industrial process for the production of chlorine gas and sodium hydroxide from NaCl brine. The primary reactions are[56]:



Due to the potential used water is also oxidized at the anode, though this reaction is slow due to sluggish kinetics:



In this process chlorine gas is the desired product and side reactions are minimized by maintaining acidic conditions at the anode (chlorine evolving side). This is achieved by membrane separation of the chlorine and hydroxide half-cells. While the chlor-alkali process has been heavily researched and the reactions are the same as the electrochemical antifouling reactions, the work has been to optimize production. Under the contrasting basic conditions present in open seawater, chlorine gas disproportionates, forming chloride and hypochlorite. This can be viewed either as a sequential homogenous reaction or, due to the fast rate, is often lumped in with the chlorine generation reaction as given in Equation 2.7.4.



This reaction has in the past been considered as a part of the proposed mechanism of Equation 2.7.1 [57]. The pKa of hypochlorous acid is 7.53, therefore at pH

= 8 as in seawater, hypochlorous acid and hypochlorite exist in equilibrium with a ratio of about 3:1 [30]. These species are metastable in water in the dark, but sunlight promotes decomposition to the only thermodynamically stable chlorine species in water, chloride [58]. Chlorate generation is a possible side reaction due to the presence of hypochlorite and hypochlorous acid, as in Equation 2.7.5.



This homogenous reaction is rather slow, and in practice reactor space-time is provided to allow the reaction to reach completion [59]. In open ocean conditions, with dilution and organic material to react with, this is unlikely to be of concern.

Higher order electrochemical oxidation of chlorine is possible, and thermodynamics favors disproportionation of oxidized chlorine species [30], however the existence of the chlor-alkali industry suggests that kinetic limitations favor lower oxidation state species.

2.8 Electrochemistry Overview

Kinetics:

The well-known Butler-Volmer equation, Equation 2.8.1 describes the kinetics of a reversible electrochemical reaction.

$$i = i_0 \left[e^{\frac{\alpha_{an} n F (E - E_{eq})_{red}}{RT}} - e^{\frac{\alpha_{cat} n F (E - E_{eq})_{ox}}{RT}} \right] \quad \text{Equation 2.8.1}$$

Where i is the current at the electrode surface, i_0 is the exchange current, α is the anodic or cathodic charge transfer coefficient, n is the number of electrons transferred in the redox half-reaction, F is Faraday's constant, E is the electrochemical potential at the electrode, E_{eq} is the equilibrium potential found using the Nernst equation, R is the universal gas constant, and T is temperature. The term $\alpha n F (E -$

E_{eq}) is similar to the activation energy for the reaction. The subscripts red and ox denote that the equilibrium potentials are for the reduction and oxidation reaction, respectively, as both the forward and reverse reactions are accounted for.

When one reaction dominates due to a sufficient overpotential the Butler-Volmer equation reduces to the Tafel Equation, Equation 2.8.2.

$$i = i_0 \left[e^{\frac{\alpha n F (E - E_{eq})}{RT}} \right] \quad \text{Equation 2.8.2}$$

Equilibrium:

The Nernst Equation, Equation 2.8.3, describes the equilibrium potential of a chemical system in terms of reduction potential.

$$E_{red,eq} = E^0_{Red} - \frac{RT}{nF} \ln \frac{a_{Red}}{a_{Ox}} \quad \text{Equation 2.8.3}$$

Where E^0_{Red} is the standard reduction potential of the system, and a_i are the activities of the reduced and oxidized species. The difference between the electrode potential and the equilibrium potential is the driving force for chemical reaction.

Electrochemical Methods:

The charge transfer coefficient and exchange current density are important kinetic parameters which determine “how good” an electrode is for performing a given electrochemical reaction. They are characteristics of the chemical reaction being driven and the electrode surface catalyzing the reaction paired as a system. The exchange current density is the amount of current flowing at equilibrium. This value embodies the number of available surface sites for adsorption, as well as the interaction energy of chemical species with those sites. The physical interpretation of the charge transfer coefficient is the ratio of the change in ground state energy to the change in intermediate state energy when subjected to an electric field. Alternatively it may be

viewed as the amount of applied energy which goes to reducing the activation energy barrier of the limiting reaction step. This is depicted in Figure 2.8.1.

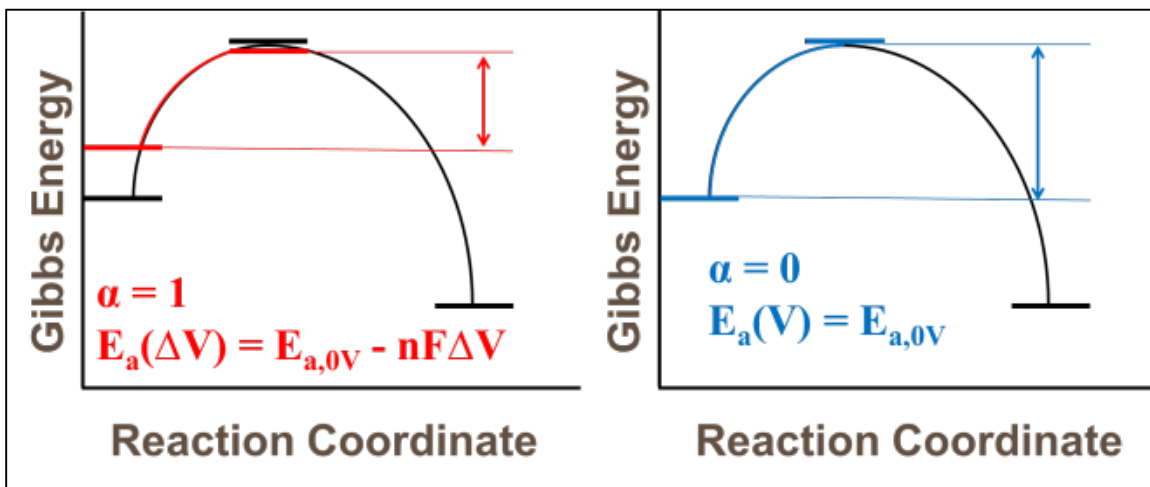


Figure 2.8.1. Physical interpretation of charge transfer coefficient. At left, $\alpha=1$ and the activation energy, E_a is reduced by the full amount of energy applied, $nF\Delta V$, where nF converts the energy applied in volts to Joules in standard reaction coordinates. At right $\alpha=0$ and the reaction cannot be catalyzed electrochemically. Electrochemical reactions lie between the bounds of these extremes.

From a mathematical viewpoint it is clear that high exchange current density and a charge transfer coefficient near 1 are desired to increase reaction rate without necessitating high over-potentials. Both parameters are critical to know when designing any electrochemical system, and are often measured to determine corrosion rates of metals.

ASTM International provides a standard set of conditions for measuring the Tafel model kinetic parameters of metallic corrosion [60]. The standard calls for a potentiodynamic sweep progressing from the corrosion potential moving towards +1.6V vs saturated calomel electrode (SCE) at a rate of 0.6V/h (0.167mV/s). Kinetic parameters are found by analysis of the resulting voltage-current plot, as in Figure 2.8.2.

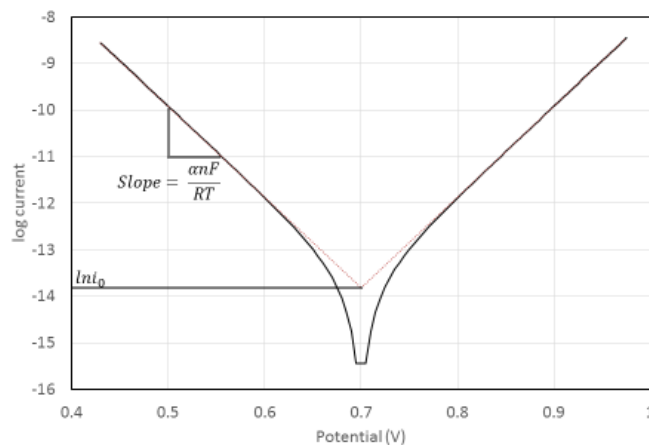


Figure 2.8.2. An ideal Butler-Volmer plot with equilibrium potential of 0.7V. The slope of the $\ln(i)$ vs V plot in the linear regime gives the charge transfer coefficient, while the extension of that line to the equilibrium potential gives the exchange current density.

The impact of scan rate and directionality of the scan have been analyzed for titanium alloy corrosion in seawater analogue [61]. It was shown that significant skewing may result from a poor choice of scan rate, with accurate results achieved using 0.1mV/s scan rate, with scan progressing towards more positive potential, consistent with the ASTM standard.

The Butler-Volmer and Tafel equations assume that the system is reaction rate limited, rather than mass transport limited. This is seldom the case for real systems with reactions involving species in the bulk. When mass transfer limits the reaction rate, the current becomes Equation 2.8.4.

$$i = nFN_{limit} \quad \text{Equation 2.8.4}$$

Where n is the number of electrons given to or removed from a species and N_{limit} is the flux of the limiting reagent at the electrode surface.

Mass transport of charged species is described by migration due to electric field, diffusion, and convection as in Equation 2.8.5 [62].

$$N_i = -z_i \mu_i F c_i \nabla \Phi - D_i \nabla c_i + c_i v \quad \text{Equation 2.8.5}$$

The electrostatic potential gradient, $\nabla \Phi$, is the negative of the electric field. The charge of the species is denoted by z_i , while the species mobility is given by μ_i . In characterization studies migration can be effectively eliminated due to charge shielding by using sufficiently concentrated electrolytes. The remaining flux is described by Equation 2.8.6 [63].

$$N_i = c_i v_i - D_i \nabla c_i \quad \text{Equation 2.8.6}$$

Where D is the species diffusion coefficient, c_i is the species concentration, and v is the bulk fluid velocity. Well characterized convective conditions are often designed to allow experiments to measure kinetic parameters, diffusion coefficients, and/or electrode areas.

Several highly studied systems have well characterized hydrodynamics which are used for studying electrochemical reactions. For the well characterized hydrodynamics of a rotating disk electrode under mass transport limitation, this yields the Levich Equation, Equation 2.8.7 [64].

$$i_l = 0.6205 F n A \nu^{-\frac{1}{6}} D^{\frac{2}{3}} \omega^{\frac{1}{2}} C_{bulk} \quad \text{Equation 2.8.7}$$

Where i_l is the total mass transport limited current, A is the area of the electrode where the limiting reagent is reacting, ν is the kinematic viscosity of the electrolyte solution, D is the diffusion coefficient, ω is the rotation speed, and C_{bulk} is the bulk concentration of the limiting reagent [63]. Recognizing that the mass transport rate must be equal to the rate of transport due to reaction gives Equation 2.8.8.

$$\frac{i}{nFA} = k(C_{bulk} - C_{surface}) \quad \text{Equation 2.8.8}$$

Where k is the mass transfer coefficient, and the surface concentration is taken as 0 for the extreme limit. The boundary layer thickness is characterized for a rotating disk, and taking a steady state diffusion model gives Equations 2.8.9-11.

$$k = \frac{D}{\delta} \quad \text{Equation 2.8.9}$$

$$i_l = nFA \frac{D}{\delta} C_{bulk} \quad \text{Equation 2.8.10}$$

$$i_l = nFA \frac{D}{1.61\nu\omega^{1/2}D^{2/3}} C_{bulk} \quad \text{Equation 2.8.11}$$

In the intermediate case the surface concentration of reactant is not entirely depleted, yet is reduced enough to affect the reaction rate. In such a case, surface concentration can be used to link the mass transport limited with the kinetic limited current, giving the resultant current described by the Koutecky-Levich equation, Equation 2.8.12 [64].

$$\frac{1}{i} = \frac{1}{i_l} + \frac{1}{i_K} \quad \text{Equation 2.8.12}$$

It is critical for this treatment to note that the kinetic limited reaction rate expands the exchange current density from the Butler-Volmer and Tafel models and gives it in the more general form of Equation 2.8.13 with $\alpha = \alpha_{cat} = 1 - \alpha_{an}$ assumed.

$$i_0 = F A k_0 C_{ox,surface}^{(1-\alpha)} C_{red,surface}^{\alpha} \quad \text{Equation 2.8.13}$$

The term k_0 is a standard rate constant with dimension Length/time, and the concentrations are those at the electrode surface. For the one-step, one-electron process, with negligible reverse current, the math works out to Equation 2.8.14.

$$i = \frac{FAk_f C_{ox,bulk}}{1 + k_f \delta / D} \quad \text{Equation 2.8.14}$$

The term k_f is the forward rate constant for reduction given in Equation 2.8.15.

$$k_f = k_0 e^{\frac{\alpha_{an} F (E - E_{eq})_{red}}{RT}} \quad \text{Equation 2.8.15}$$

Many other electrode designs may be implemented to ascertain kinetic parameters, as long as the hydrodynamic boundary layer is well defined.

2.9 Microchannel Reactor Design

While rotating disk electrodes are often used for kinetic analyses due to the well-established mass transport model, a possibly superior method utilizes microchannel reactor technology. The nature of microchannel devices, those with length scales on the order of 1mm, ensures that flow is laminar over a large range of flowrates. Laminar flow conditions eliminate the need for convective mass transport correlations and enable accurate modeling of mass transport from first principles. Kinetic studies with flow-through reactors also enable on-line analysis of reaction products, such as with colorimetry or mass spectrometry. These considerations make microchannel devices a good choice for precise kinetic analysis. An added bonus of micro-architecture electrochemical systems is that accuracy of electrochemical measurements is increased as size decreases, due to reduction of iR power losses, both in electronics and the test system.

A great deal of research effort has been invested into the study of microchannel device architecture. Flow distribution is a significant issues in reactor design. Trapezoidal

geometry with channel walls breaking up the flow has been shown to be effective at distributing flow [65].

2.10 Graphite Composite Electrodes and Conduction in Thin Composite Films

Graphite is a common electrode material due to its high conductivity, relative inertness, and low cost. It is often mixed into a binding matrix, such as a wax or paint, to create electrodes of complex geometry. This has been done with a polyurethane matrix applied to PET film in demonstration of electrochemical antifouling performance [27].

Percolation Theory

Conduction in graphite filled polymers has been observed to follow percolation theory, i.e. resistance is very high until a critical volume percent (CVP) is reached, at which point further conductive filler produces marginal decreases in resistance [1, 66]. This affect arises due to the high conductivity of graphite filler and comparatively low conductivity of the paint binder. At low graphite loading the binder bulk resistance dominates and the film is highly resistive. The CVP is reached when pigment particles are packed in the film such that they just touch, as shown in Figure 2.10.1.

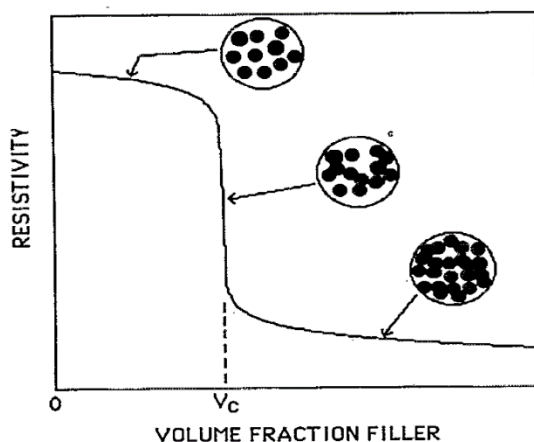


Figure 2.10.1 Resistivity of composite material as function of conductive filler volume fraction. When filler particles begin to touch and form conductive pathways, the bulk resistivity of the materials shows a precipitous drop. Figure used with permission [66].

Sheet Resistance

The resistance to current flowing through a medium is given by Equation 2.10.1.

$$R = \rho \frac{L}{wt} \quad \text{Equation 2.10.1}$$

Where ρ is the bulk material resistivity, L is the length of film parallel to current flow, t is the film thickness, and w is the film width. Because film thickness and bulk resistivity are difficult to measure, the resistance across a thin film resistor is characterized by the sheet resistance, R_{sh} , as given in Equation 0.2.

$$R = \frac{\rho L}{tW} = R_{sh} \frac{L}{W} \quad \text{Equation 2.10.2}$$

A four-point-probe method has been shown to be effective at measuring sheet resistance of graphite filled polymer films, with results compared to those obtained using a transfer length method [1]. A four point probe, shown schematically in Figure 2.10.2, utilizes four equally spaced probes to make accurate measurements with minimal iR voltage effects.

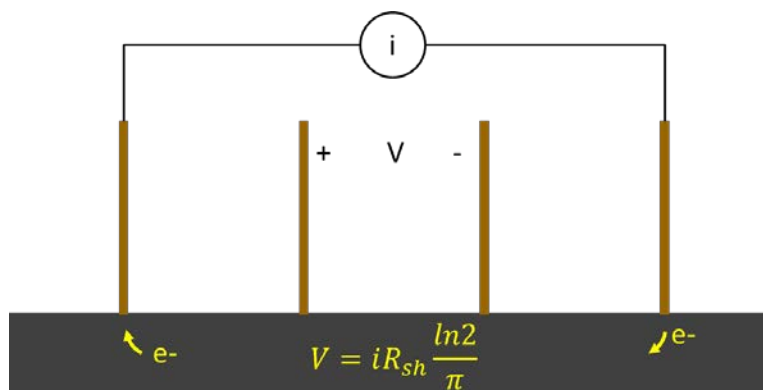


Figure 2.10.2 Diagram of a 4 point probe. A measured current, i , is applied to the exterior probes. The voltage, V , across the interior probes is measured and, neglecting edge effects, the sheet resistance is given by Equation 0.3 [67].

$$R_{sh} = \frac{\pi V}{\ln 2 i} \quad \text{Equation 2.10.3}$$

2.11 Graphite Electrode Degradation

The Tafel equation is useful for describing a reaction driven with about 50mV or more overpotential. There are two electrode specific parameters which must be evaluated for the system of interest: i_0 and α . The exchange current density, i_0 , relates to the number of sites available on the electrode surface for reaction, and how rapidly species adsorb and desorb from the surface, while the charge transfer coefficient, α , is related to how well the surface site catalyzes the desired reaction. Graphite particles have two types of sites: edge sites where graphene sheets terminate, usually in oxide groups, and basal sites on the surface of graphene sheets. As different sites will have different electrochemical effectiveness, how kinetic parameters change with electrode use will provide insight to the dominant degradation mechanism. Delamination of sheets due to repeated intercalation/de-intercalation cycles and carbon oxidation to CO₂ are the likely culprits of degradation [56, 68, 69]. Intercalation causing graphite grains to swell and dislodge from the surface is also possible.

Previous chronoamperometric degradation studies have been completed with sintered graphite rods in zinc-bromide electrolyte [70]. The charge transfer coefficient for oxidation was measured to be near the ideal value of 0.5, with little change after 300A-h/cm² of anodic aging current. The cathodic charge transfer coefficient was measured to be lower initially, near 0.2, but showed improvement with aging. The exchange current density decreased from an initial value of about 7mA/cm² to about 3.5mA/cm² after 300A-h/cm² of aging.

2.12 The 1-D Terminal Effect Model

When the resistance to current flow in an electrode is much less than the resistance to current flow in the electrolyte, it is assumed that the electrode is at a uniform potential with uniform charge density. Many cases exist, however, where the

resistance of the electrode material itself is not negligible, and a voltage gradient forms in the electrode causing non-uniformity in charge density [71]. This effect is called the terminal effect and is depicted in Figure 2.11.1.

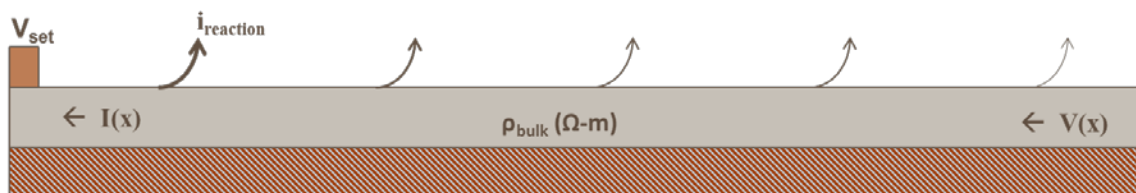


Figure 2.11.1 Resistive electrode with insulating backing. Voltage is greatest near the contact point. Ohmic loss in the material causes a voltage profile to develop, resulting in lower current density away from the contact.

Due to the non-linear response of electrochemical kinetics to potential, analytical solutions are rare and numerical solutions are often utilized [72]. For the case of non-plating planar electrodes with an assumed 1-D voltage profile and Tafel kinetics, the voltage and current distribution has been solved for [73].

The analysis begins with the statement that the derivative of current is the reaction current, which is justified by charge conservation, as in Equation 2.11.1.

$$\frac{\partial i}{\partial x} = w i_0 e^{bV} \quad \text{Equation 2.11.1}$$

Where Tafel kinetics have been assumed, w is the width of the electrode, $b \equiv \frac{\alpha n F}{RT}$, and V is the local overpotential. Taking the derivative of Equation 2.11.1 gives Equation 2.11.2.

$$\frac{\partial^2 i}{\partial x^2} = \frac{\partial i}{\partial x} b \frac{\partial V}{\partial x} \quad \text{Equation 2.11.2}$$

Applying Ohm's law in differential form (Equation 2.11.3) gives a differential equation in current only, Equation 2.11.4.

$$\frac{\partial V}{\partial x} = \frac{\rho}{wt} i \quad \text{Equation 2.11.3}$$

$$\frac{\partial^2 i}{\partial x^2} = \frac{b\rho}{wt} i \frac{\partial i}{\partial x} \quad \text{Equation 2.11.4}$$

Here ρ is the electrode material bulk resistivity, w is the electrode width, and t is the electrode thickness. Integration gives Equation 2.11.5.

$$\frac{\partial i}{\partial x} = \frac{b\rho}{2wt} i^2 + C_1 \quad \text{Equation 2.11.5}$$

Assuming that no current leaves the end of the electrode in the x-direction the boundary condition $i|_{x=0} = 0$ gives Equation 2.11.6

$$C_1 = wi_0 e^{bV}|_{x=0} \quad \text{Equation 2.11.6}$$

Or applying the boundary condition $i|_{x=L} = i_{total}$ gives Equation 2.11.7.

$$C_1 = wi_0 e^{bV}|_{x=L} - \frac{b\rho}{2wt} i_{total}^2 \quad \text{Equation 2.11.7}$$

Integration of Equation 2.11.5 gives Equation 2.11.8

$$\sqrt{\frac{2}{\frac{b\rho}{wt} C_1}} \arctan\left(i \sqrt{\frac{b\rho}{wt} \frac{1}{2C_1}}\right) = x + C_2 \quad \text{Equation 2.11.8}$$

Again applying $i|_{x=0} = 0$ gives $C_2 = 0$. Solving for current gives Equation 2.11.9.

$$i = \sqrt{\frac{2wtC_1}{b\rho}} \tan\left(\sqrt{\frac{b\rho C_1}{2wt}} x\right) \quad \text{Equation 2.11.9}$$

The total current flowing through the electrode can be measured and yields C_1 by Equation 2.11.10.

$$i|_{x=L} = \sqrt{\frac{2wtC_1}{b\rho}} \tan\left(L \sqrt{\frac{b\rho C_1}{2wt}}\right) \quad \text{Equation 2.11.10}$$

3. Materials and Methods

3.1 Graphite Paints

Paints used in this research were mixed at 55 dry weight percent graphite unless otherwise stated. The base paint was Minwax Fast Drying Polyurethane in Clear Gloss, from The Home Depot. The weight retention upon curing was measured to be 50%. The graphite filler was Sigma Aldrich product number 282863 Graphite, powder, <20micron, synthetic, used as received. Paint was added to graphite in 20mL scintillation vials. A vortex mixer was used to achieve consistent mixing. Mix time was 2 minutes minimum.

Paint durability and applicability depend on the graphite loading. To determine the range of graphite loading to consider, several paints were prepared, ranging from 35-60% graphite by weight on the assumed basis of 75% solids in the polyurethane paint. Consistency was noted and paints were applied to an insulating fiberglass board using the blade method with painter's tape (3M Scotch Blue 2093EL, ~0.10mm thick) as in Figure 3.1.1.

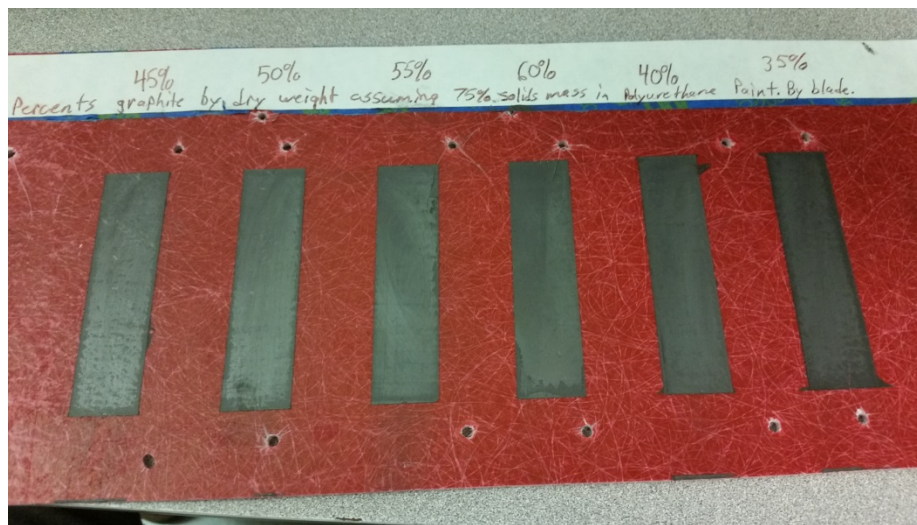


Figure 3.1.1 Graphite paint samples applied to insulated fiberglass backing.

The sheet resistance was measured and recorded for each sample. Samples of polyurethane paint were placed in plastic weighing trays and left to cure in a vacuum oven for two weeks to determine the actual weight retention.

3.2 Sheet Resistance Measurement

Sheet resistance was measured using the 4-point-probe (4PP) method. A 1x4 spring loaded contact (DigiKey PN ED90476-ND, Figure 3.2.1) was used to provide equally spaced contacts with uniform pressure.

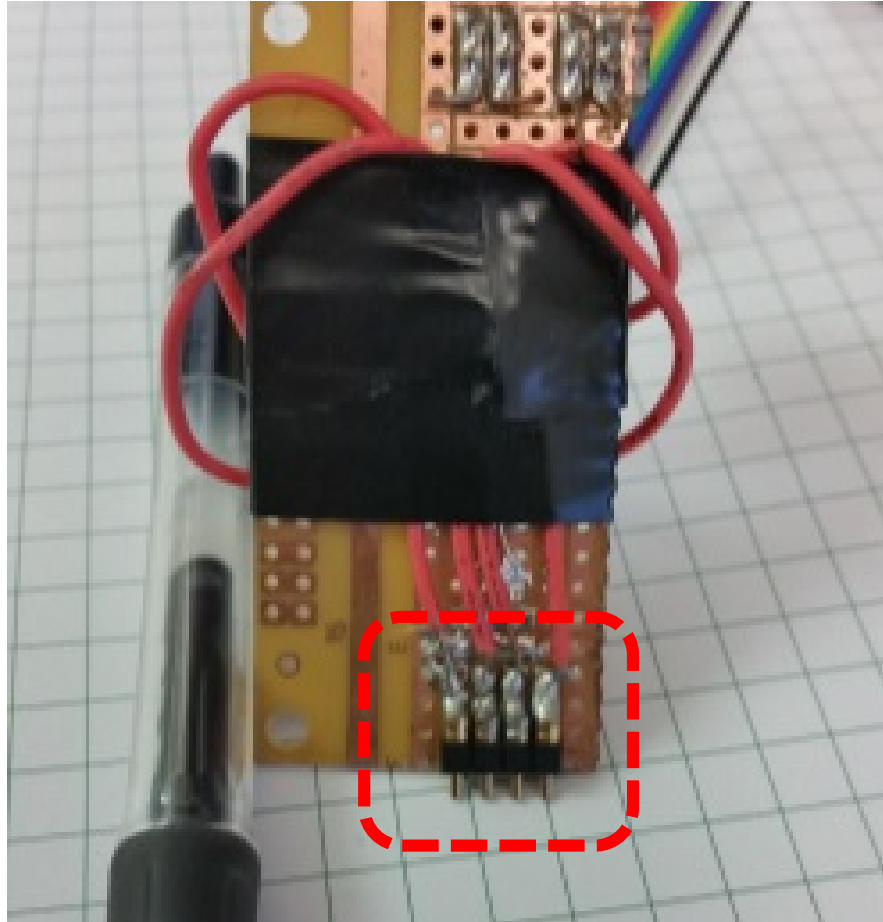


Figure 3.2.1 The spring loaded contact with uniformly spaced probes provided repeatable contacting for 4PP measurements, highlighted by the red dashed rectangle. Pen and quarter inch grid paper for size reference.

A 5V regulator circuit was built with a changeable current sense resistor in the 5V circuit, which ran to the exterior probes. The sense resistor also adds a series resistance which impacts the current delivered. The interior probes were routed directly to a voltage meter. The voltage across the sense resistor and interior probes was measured and the sheet resistance was calculated as in Equation 3.2.1.

$$R_{sh} = \frac{\pi}{\ln 2} V \frac{R_{sense}}{V_{sense}} \quad \text{Equation 3.2.1.}$$

3.3 Electrolytes

Chloride electrolytes were prepared with NaCl at 35g/L (BDH). Hypochlorite was introduced at 1ppm using 20 μ L/L sodium hypochlorite solution (5% available chlorine) from J.T. Baker. The pH was buffered with 0.1M Tris(Hydroxymethyl) Aminomethane (Macron Fine Chemicals), with pH adjusted to 8.0 by addition of approximately 4.5mL concentrated HCl (Macron Fine Chemicals) per liter. A Vernier Tris-Compatible pH probe was used to verify pH. The make-up water used was building DI from Gleeson Hall.

Synthetic Seawater used in this work is the same as the chloride electrolyte previously described, with the addition of 100mg/L KBr (EMD).

Bromide Electrolytes were prepared with 35g/L KBr (EMD) and 0.1M Tris(Hydroxymethyl) Aminomethane (Macron Fine Chemicals). Bromine (Sigma Aldrich #207888) was added to 1.0mM (52 μ L/L). The pH was adjusted to 8.0 with 6.5mL/L concentrated HBr (Sigma Aldrich #268003). The make-up water used was building DI from Gleeson Hall.

Potassium ferrocyanide solutions in this work were prepared with 5mM $K_3Fe(CN)_6$, 5mM $K_4Fe(CN)_6$, and 0.5M K_2CO_3 . The make-up water used was building DI from Gleeson Hall.

Non-reactive supporting electrolyte was made with 0.60M (60.66g/L) KNO_3 (EMD) and 0.1M Tris(Hydroxymethyl) Aminomethane (Macron Fine Chemicals). The pH was adjusted with approximately 3.9mL nitric acid (EMD) per liter to pH 8. The makeup water was building DI from Gleeson Hall.

Experiments which used dye as an indicator used Brilliant Blue FCF (Fluka 80717) at a concentration of 3.88 μ M. This concentration provided sample UV-vis absorbance of approximately 0.7 at 630nm in a 1.0cm path flow cell (Avantes Micro flow Z-cell-10) with

18 μ L dead volume. Electrolytes with dye were prepared without NaOCl or Br₂, as these would degrade the dye and be consumed.

3.4 Area Determination

Electrochemically active surface area was analyzed on a graphite paint electrode. The graphite paint was applied to the exterior of a ¼ inch PVC tube. Silver filled epoxy (MG Chemicals #8331) was used to attach a wire lead. The tip of the working electrode was submerged in a Dr. Bob's Electrochemical Cell, wetting approximately 50mm² of the surface. Potassium ferrocyanide electrolyte was used with N₂ purging and blanket gas. The reference electrode used was Ag|AgCl in 1M KCl, the counter was a ¼ in graphite rod. Cyclic voltammograms at scan rates of 20-200mV/s were run and the area was found by applying the Randles-Sevcik equation, Equation 3.4.1[74].

$$i_{peak} = 0.4463nFAC_{bulk} \left(\frac{nFvD}{RT} \right)^{1/2} \quad \text{Equation 3.4.1}$$

Due to the results found, geometric area was used for the remainder of this work.

3.5 Voltage Profile Experiments

Voltage profile data was taken from previous work, in which graphite paint electrodes were prepared on Acrylic substrates, with voltage sense probes attached from the back-side [1]. One end of the electrode was held at a set potential in synthetic seawater using a Gamry Reference 3000 potentiostat and the resulting voltage profile along the length of the electrode was measured. The previous work utilized a numerical solution to solve for the Tafel Model kinetic parameters for individual plates. This was expanded upon by applying the analytical solution of the 1-D terminal effect model to the data and minimizing the sum of squared errors using the Microsoft Excel Solver feature to determine the kinetic parameters with greater confidence. The sheet resistance of each electrode was taken as a fitting parameter and compared to

measured values. In previous work, a similar 55 wt% graphite paint electrode was held at 1.1V vs Ag|AgCl in a filtered seawater tank at Hatfield Marine Science Center, and the observation was made that due to the terminal effect, antifouling efficacy extended 6 inches below the air-water interface [1]. This work expanded upon these findings by applying the 1-D terminal effect model with the identified kinetic parameters and measured sheet resistance to determine the potential at the threshold of antifouling performance. Figure 3.3.1 shows the field experiment at the conclusion of the test.

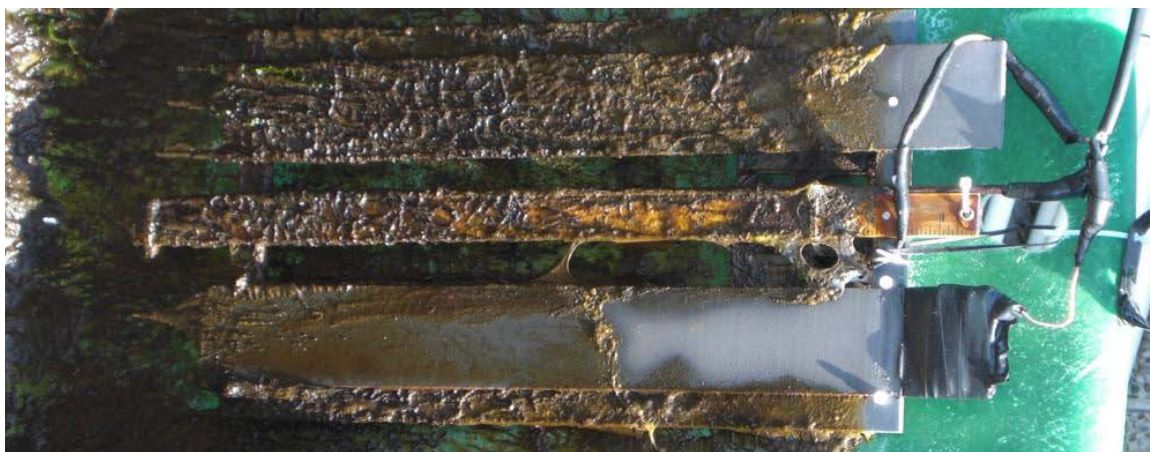


Figure 3.3.1 with permission from previous work by Matthew Delaney[1]. With one end of the electrode held at 1.1V vs Ag|AgCl, protection from fouling was observed to a depth of 7 inches. At 6 inches fouling is present on the edge, but likely due to a more resistive thin area of paint. Sheet resistance was $47\Omega/\square$.

Expanding upon the previous research a similar experiment was conducted in the open ocean, mounted to the Ocean Sentinel instrumentation buoy deployed by the Northwest National Marine Renewable Energy Center. A battery powered, field deployable potentiostat was built to provide power to a 2ft x 2in conductive film applied to a 2ft x 4in acrylic substrate. The voltage and current provided to the system were recorded using Omega OM-EL-USB-3 voltage data loggers. The conductive film was applied using the blade coating technique. Lands for the blade were made by applying two layers of 1in wide masking tape (3M Scotch) to the acrylic substrate to create a well of $\sim 250\mu\text{m}$. Photos of the deployment are given in Figure 3.3.2.

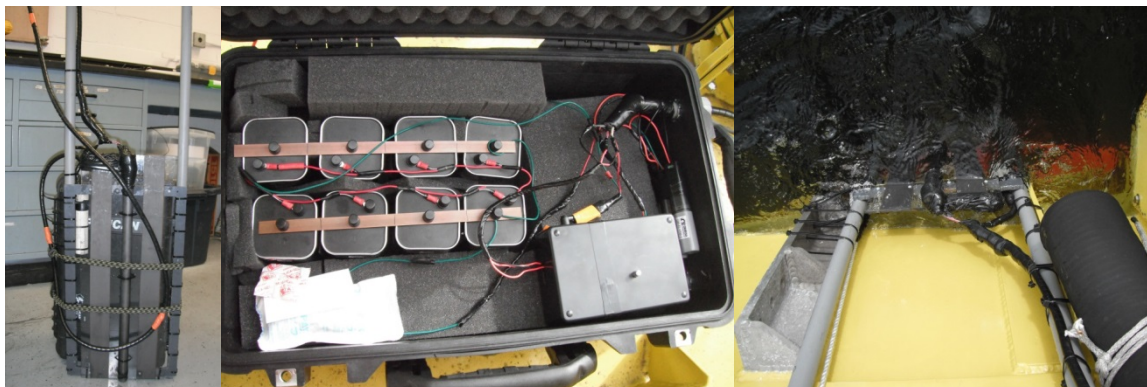


Figure 3.3.2 Ocean Sentinel voltage profile experiment. Left: Test plates with control at right and the test plate at left. The white PVC tube protects the Ag|AgCl reference wire from degradation due to sun light, the graphite rod in the center is the counter electrode. Middle: Battery pack with data loggers and in-house built potentiostat. Right: Experiment deployed on the Ocean Sentinel buoy.

The voltage was set at 1.5V vs Ag|AgCl with an inexpensive in-house built potentiostat. The potential is controlled with a trim resistor. The circuit diagram is given in Figure 3.3.3.

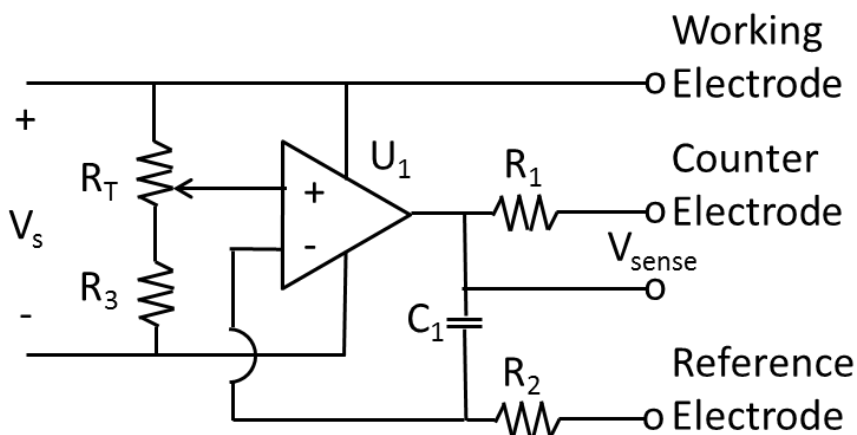


Figure 3.3.3 Simple in-house built potentiostat circuit diagram. R₁ is a 10Ω sense resistor. By measuring the voltage across R₁, the current flowing through the system is measured. R_T is a 5kΩ trim resistor used to set the working electrode potential, R₂ is a 10MΩ resistor meant to stop current from flowing through the reference and causing damage. R₃ is a 4kΩ resistor which adjusts the voltage range possible to select. C₁ is a 100nF ceramic disk capacitor which damps overshoot of the response. U₁ is an LM358AN op-amp.

3.6 Analytical Solution of Terminal Effect Model and Voltage Profile Analysis

Given the data on hand, the terminal effect would be very useful to have modeled in terms of voltage. In this analysis $x=0$ is the point where the voltage is set, and $x=L$ is the far end of the electrode, where no current flows through the paint electrode. Combining Ohm's Law, Equation 2.11.3, and Equation 2.11.1 gives Equation 3.6.1.

$$\frac{\partial^2 V}{\partial x^2} = \frac{\rho}{t} i_0 e^{bV} \quad \text{Equation 3.6.1}$$

Multiplying both sides by dV/dx and integrating with respect to x gives Equation 3.6.2.

$$\frac{1}{2} \left(\frac{\partial V}{\partial x} \right)^2 = \frac{\rho i_0}{t b} e^{bV} + C_1 \quad \text{Equation 3.6.2}$$

Where C_1 is a constant of integration. At $x=L$ there is no current, and therefore $dV/dx = 0$, which gives C_1 as $-\frac{\rho i_0}{t b} e^{bV} |_{x=L}$. Taking the square root and rearranging gives Equation 3.6.3.

$$\frac{\frac{\partial V}{\partial x}}{\sqrt{\frac{2\rho i_0}{t b} e^{bV} + C_1}} = \pm 1 \quad \text{Equation 3.6.3}$$

Taking the integral of both sides of the equation with respect to x gives Equation 3.6.4.

$$\frac{\sqrt{2} \tanh^{-1} \left[\frac{\sqrt{\frac{\rho i_0}{t} e^{bV} + bC_1}}{\sqrt{bC_1}} \right] \sqrt{\frac{\rho i_0}{t} e^{bV} + bC_1}}{b^{3/2} \sqrt{C_1} \sqrt{\frac{\rho i_0}{t} e^{bV} + C_1}} = C_2 \pm x \quad \text{Equation 3.6.4}$$

Simplifying with C_1 gives Equation 3.6.5.

$$-\frac{\sqrt{2} \tanh^{-1} \left[\frac{\sqrt{(e^{bV} - e^{bV}|_{x=L})}}{\sqrt{-e^{bV}|_{x=L}}} \right]}{\sqrt{\frac{b\rho}{t} i_0} \sqrt{-e^{bV}|_{x=L}}} = C_2 \pm x \quad \text{Equation 3.6.5}$$

In terms of the inverse tangent this becomes Equation 3.6.6

$$\frac{\sqrt{2}}{\sqrt{\frac{b\rho}{t} i_0} \sqrt{-e^{bV}|_{x=L}}} \frac{\tan^{-1} \left[i \frac{\sqrt{(e^{bV} - e^{bV}|_{x=L})}}{\sqrt{-e^{bV}|_{x=L}}} \right]}{i} = -C_2 \pm x \quad \text{Equation 3.6.6}$$

Which simplifies to Equation 3.6.7

$$\frac{\sqrt{2}}{\sqrt{\frac{b\rho}{t} i_0} e^{bV}|_{x=L}} \tan^{-1} \left[\frac{\sqrt{(e^{bV} - e^{bV}|_{x=L})}}{\sqrt{e^{bV}|_{x=L}}} \right] = C_2 \pm x \quad \text{Equation 3.6.7}$$

At $x = L$, $V = V_{x=L}$, such that C_2 is given by Equation 3.6.8.

$$C_2 = \pm L \quad \text{Equation 3.6.8}$$

Finally solving for V gives Equation 3.6.9.

$$V = V|_{x=L} + \frac{1}{b} \ln \left[\sec^2 \left((x - L) \sqrt{\frac{b\rho}{2t} i_0 e^{bV}|_{x=L}} \right) \right] \quad \text{Equation 3.6.9}$$

The voltage at the end of the electrode is determined from Equations 2.11.6 and 7, and the total current flowing through the test electrode. The charge transfer coefficient and exchange current densities were then determined by fitting voltage profile data to the model. Using the determined parameters the voltage at the boundary of fouling prevention in field experiments is reported.

3.7 Discrete Voltage Profiling

To build upon the voltage profile results, a discrete voltage profile experiment was developed. A device was fabricated with 9 parallel flow channels, each of which had the components of an electrochemical cell: a working electrode, a counter electrode, and a reference electrode. The device had a clear acrylic top to allow sunlight to pass and enable algae growth. The channels are half-inch deep by 2 inches wide, with 3 inch long segments for the working electrodes and 4 inch long segments for the counter electrodes. The overall dimensions were 1ft x 2ft and the material chosen was HDPE (McMaster-Carr) as shown in Figure 3.7.1

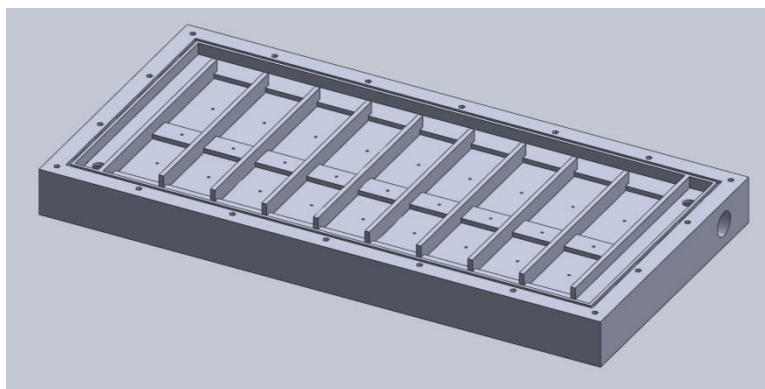


Figure 3.7.1 Parallel channel flow reactor design.

Holes for electrical contacts were $1/16''$. The counter and working electrodes were made by soldering copper wire to copper clad PCB blanks (Radio Shack) to distribute voltage, which were cut to the dimensions of the wells. The blanks were then epoxied (West Systems 105 resin, 205 fast hardener) into place and the surfaces were

coated with graphite filled paint. The same epoxy was used to seal and secure wires in their holes. Painted surfaces were polished with sandpaper down to 1500grit. To enhance flow distribution a baffle was fabricated from polycarbonate and placed across the channel inlet. Two 3/16in holes were drilled for each channel inlet. Reference electrode frits were created by cutting the barrier section of 100 μ L auto pipette barrier tips and pressing them into the reference electrode holes. Female Luer Lock fittings were epoxied and/or glued (West Systems 105 Resin, 205 fast hardener, Loctite 431 superglue) in place on the bottom side of the device to enable a removable seal for silver chloride wire insertion. Silver wire (0.999, 0.020in) was rinsed with 0.1M HNO₃ followed by 18 M Ω cm DI water, then oxidized in 1M KCl for 30 minutes at 0.4mA/cm² to generate Ag|AgCl reference electrode wires. These wires were soldered to copper wire, and epoxied into male Luer Lock fittings. The device was sealed with silicone gasket maker throughout (Permatex Blue RTV) and screws around the exterior. One channel was left uncharged as a control. The remaining channels were held at various potentials using a series of 8 custom built potentiostats powered by a bank of 8 Energizer 6-Volt lantern batteries in parallel. Each channel had a 1k Ω current sense resistor in series with the counter electrode, and used an Omega OM-EL-USB-3 voltage data logger to measure the voltage, and therefore current flowing through the system. Electronics were housed in a Pelican case with desiccant to protect from corrosion.

Prior to deployment, flow distribution was checked by injection of methylene blue into the feed line in the lab. A still shot of the result can be seen in Figure 3.7.2.



Figure 3.7.1 Methylene blue injection into feed results in fairly even distribution.

The device was deployed at Hatfield Marine Science Center with a feed from the filtered seawater line there. Flow rate was measured with a 5 gallon bucket and a stopwatch. The experiment was left to run for 20 days. The fouling results were compared with the concentrations expected based on COMSOL modeling results. The applied potentials are listed in Table 3.7.1.

Table 3.7 Table of applied potentials in parallel potentiostatic flow cell experiment. Channels 3 and 4 were set in the lab, electrolyte penetration in the field took longer than expected and therefore measurements were not acquired at the time of deployment.

Channel	1	2	3	4	5	6	7	8
Voltage (V vs Ag AgCl)	1.294	1.124	1.11*	1.21*	1.181	0.991	1.105	1.275

3.8 Non-Graphitic Materials

Titanium nitride is of interest as a conductive filler which may be more durable than graphite fill. TiN was mixed with epoxy (West Systems 105 resin, 205 fast hardener) at 69% on dry weight basis and applied to 2" by 6" insulating fiberglass boards. A second set was made with 73% TiN by dry weight in polyurethane paint. Wire leads were

attached with silver epoxy (MG Chemicals #8331) and coated over with silicone.

Samples were set at 4.99V vs Ag|AgCl with custom built potentiostats.

Transparent antifouling coatings are desirable for ongoing undersea monitoring efforts[75]. Indium tin oxid (ITO) can be deposited as a conductive transparent thin film. ITO coated PET sheet (Sigma Aldrich 639303 $60\Omega/\square$ on 5mil sheet) was cut into 2in x 6in strips. Copper wires were attached to one end using conductive silver epoxy (MG Chemicals #8331). The electrical contact was sealed using silicone. Strips were held at 2.22V and 2.35V vs Ag|AgCl in seawater using custom built potentiostats.

Each test panel had a corresponding blank with no voltage applied. The test panels were deployed in filtered seawater tanks at Hatfield Marine Science Center in Newport Oregon. Observations were made after six days. The test panels and frame are shown in Figure 3.8.1

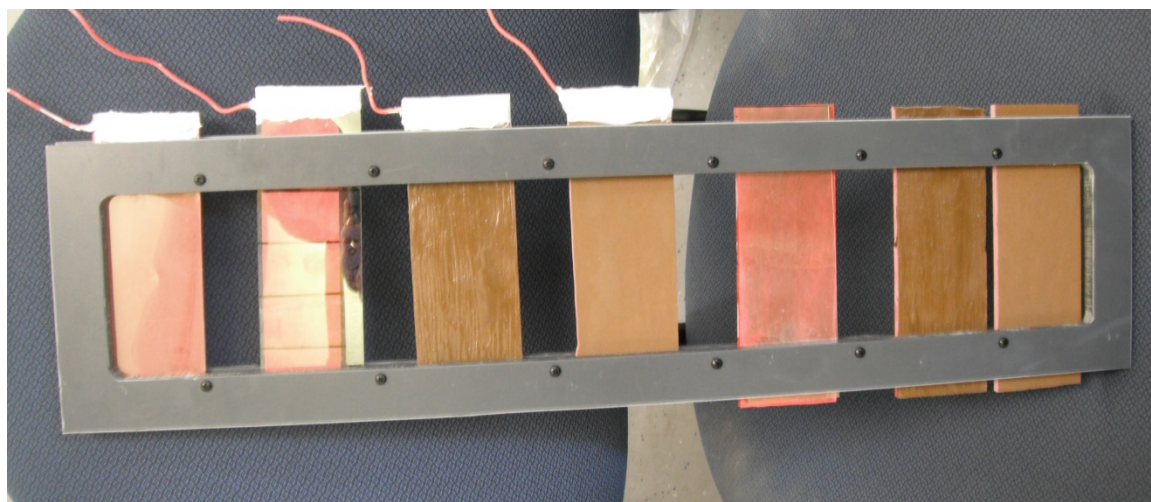


Figure 3.8.1 Test of alternative materials for electrochemical antifouling performance prior to deployment. From left to right: ITO, ITO, TiN epoxy, TiN polyurethane, ITO, TiN epoxy, TiN polyurethane.

3.9 Electrochemical Reactor Production

Polycarbonate bar stock (0.125in x 2in, McMaster-Carr) was machined on the Taig Micro-CNC mill shown in Figure 3.9.1.



Figure 3.9.1 Taig Micro-CNC mill used to machine reactor blanks from polycarbonate bar stock.

The initial operation cuts 0.20in x 1.5in paint wells. To facilitate electrical connectivity 3/32in holes were drilled into the center of each well. A 1/16in hole was placed near the edge of the center channel for reference electrode placement. Bolt holes and fluid inlet/outlet holes were also bored at this stage. A schematic of the reactor half at this stage is given in Figure 3.9.2

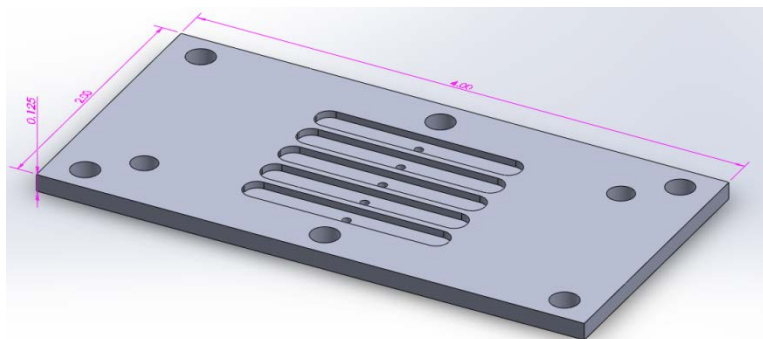


Figure 3.9.2 CAD rendering of reactor halves after first stage of machining. Curves in the paint wells are fillets due to the 3/16in end mill used.

Graphite filled paint was applied to the paint wells, with special care to ensure that the 3/32in connection holes were filled. Several layers were applied until the paint surface was nearly flush with the polycarbonate surface. Paints were allowed to dry for

a minimum of 48h. A razor blade was used to scrape any spills or excess from the surface. Silver wire (1.5mm, >0.9999, Sigma-Aldrich) was glued into the reference electrode opening with Loctite 431 formula superglue.

With glue and paint cured the second stage of machining cut a 400 μ m deep flow pocket. The pocket is trapezoid in shape, with 5 channels, each 0.02in x 1.70in, separated by fins to distribute flow. Silver conductive epoxy (MG Chemicals #8331) was used to create a bus between all pockets, and attach a copper wire lead. To create a Ag|AgCl electrode, the silver wire was rinsed with 0.1M HNO₃, followed by rinsing with high purity 18M Ω cm DI water. Then 1M KCl was dropped into the flow channel to connect the silver wire with the graphite electrode. As prescribed in Handbook of Electrochemistry[74], 0.4mA/cm² was run through the system for 30 minutes, after which the surface was rinsed with 18M Ω cm DI water, followed by soaking overnight, also in high purity DI water. Polycarbonate Luer-Lock fittings (McMaster-Carr) were glued to the inlet and outlet with Loctite Formula 431 superglue. A finished reactor half is shown in Figure 3.9.2



Figure 3.9.2 Photograph of a finished reactor half. The corners of the parallelogram have Luer Lock fittings attached. The silver dot at right is silver wire, which is oxidized in situ with 1M KCl solution fed to the reactor. The copper wire in the background is attached with silver epoxy on the reverse, with 5/32in paint filled holes enabling the contact.

To maximize signal and promote sealing, the flow was separated by semi-permeable cellulose membrane (HomeScienceTools.com) between reactor halves. To finish reactor construction, bolts were placed in their respective holes. The cellulose membrane was hydrated before being pushed down over the bolts, allowing the film to be stretched tight, before the opposing half was applied.

3.10 Electrochemical Reactor Operation

Electrolyte was purged with He continuously to degas and further passed through an HPLC mobile phase degassing unit (Alltech On-Line Degassing System 2000) before being fed to the reactor by Altex HPLC (Model 100A) pumps. Due to membrane separation, each half of the reactor was fed with a different pump to ensure a known flowrate at the working electrode. FD&C Blue #1 (Brilliant Blue FCF, Fluka 80717) was added to electrolyte at 3.88 μ M, which gives absorbance of $\sim 0.7/\text{cm}$ at 630nm. The outlet of the working electrode half of the reactor was fed through the degassing unit then routed through a UV-Vis flow cell (Avantes, 1.0cm path) for quantification. Due to the absence of chloride in some electrolytes, the built-in Ag|AgCl reference electrode was not used; a reference electrode was placed in the working electrode electrolyte feed, just before entry to the reactor. For consistency, this method was adopted for all experiments, even with chloride present.

Potentiostatic experiments were run on a Gamry Reference 3000 for 800s duration (~ 20 reactor volumes at minimum flow), with 800s of electrolyte flow with no applied potential between experiments. Except for bromide electrolyte experiments, the potential sequence used was: 1.3, 0.7, 1, 1.25, 0.95, 1.2, 0.8, 1.1, 0.9, 0.75, 0.85, 1.4V. For bromide electrolyte experiments the sequence was: 0.65, 0.7, 1, 0.55, 0.95, 0.5, 0.8, 1.1, 0.9, 0.75, 0.85, 0.6. Voltages are with respect to Ag|AgCl in 1M KCl. Each sequence was repeated 4 times for the flow rates and electrolytes tested. Dye redox activity was quantified by running non-reactive KNO_3 supporting electrolyte with dye through the cell and comparing to plain KNO_3 electrolyte results. Reaction rate was quantified both amperometrically and colorimetrically.

The system current was recorded every five seconds. The last 13 data points were averaged and used as the current value for each run. The absorption spectrum was averaged from 625nm to 635nm, with samples recorded approximately every 5 seconds. The absorption data was recorded continuously for all potentiostatic runs at a given set of conditions. The absorbance values were manually extracted by determining the last recorded point before concentration began to rise, and averaging the last 15 measurements leading to that point. Absorbance baselines had to be manually crafted as natural drift and gas bubble affects were apparent.

3.11 Aging Experiments

Test electrodes were held in 100mL 2-neck flasks filled with 120mL of electrolyte with stirring provided on a 9-well stir plate shown in Figure 3.11.1.

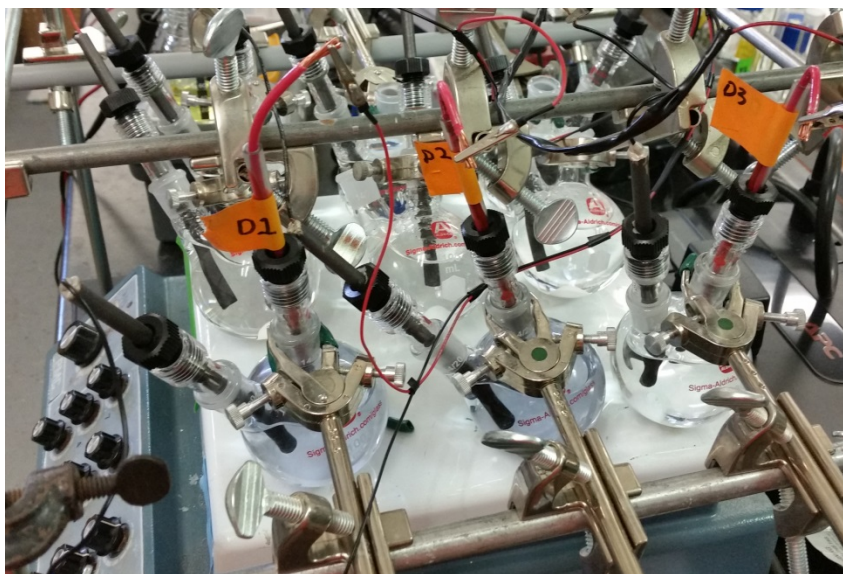


Figure 3.11.1 Galvanostatic aging apparatus.

Aging experiments utilized a custom built 9-channel galvanostat described elsewhere[70]. The counter electrodes used were 0.25in graphite rods (GraphiteStore.com). Each run consisted of aging 3 electrodes in the same electrolyte at the same current density. Test electrodes were periodically removed from the aging unit

and analyzed to determine electrochemical parameters. Blank experiments were run in the same manner without galvanostat connections.

Electrochemical parameters were analyzed using a Gamry Reference 3000 potentiostat with a Bob's Electrochemical Cell 5-neck, 50 mL flask (Gamry) shown in Figure 3.11.2.



Figure 3.11.2 Bob's Electrochemical Cell used for electrochemical measurements.

The cell has five ports: working electrode, counter electrode, reference electrode, gas/purge, and temperature ports. The counter electrode was a 0.25in graphite rod (GraphiteStore.com) and was the same throughout all tests. The reference was Ag|AgCl with 1M KCl ($V=0.235V$ vs NHE) with secondary containment. Initial runs did not utilize purging, but as the method developed, N_2 was used as purge and blanket gas, controlled by the auxiliary I/O port on the Gamry potentiostat. Temperature was monitored but did not change during runs, and only varied $\pm 2^\circ C$ between hot and cold days. Current-voltage plots for Tafel analysis were run in triplicate initially, with later methods adopting 4x operation and automatic rejection of the initial scan.

The initial aging experiments were run using $\frac{1}{4}$ " diameter graphite rods (GraphiteStore.com) as base supports, with graphite paint applied to the tip. Dual wall

polyolefin heat shrink (Raychem TAT) was used to electrically isolate the paint electrode tip in solution as in Figure 3.11.3.



Figure 3.11.3 Graphite paint electrodes prepared on graphite rods.

This sample form was convenient for controlling exposed area. Electrode tips were smoothed by slicing with a razor blade. The electrolyte used was chloride electrolyte as described in Section 3.3. The current density used was $3.16\text{mA}/\text{cm}^2$, an acceleration factor of 158x over the expected $20\mu\text{A}/\text{cm}^2$ operating condition [1].

The first run did not utilize gas purging, so oxygen reduction may have contributed noise to the data. The second and all following data sets purged with N_2 between each analysis and blanketed during analysis. A 3-way normally open solenoid valve (McMaster-Carr #7889K78) powered by an LED solid state relay (Foter SSR-25DA) was used to direct gas between purge and blanket inlets using the Gamry auxiliary I/O port.

The analysis of graphite rod supported electrodes was done using the Tafel method in Gamry Framework, which applies a staircase voltage ramp. The scans were done at $20\text{mV}/\text{s}$ with 250ms delay between setting a voltage and reading the current. The sweeps started at low potential and swept to higher potential, with manual settings to attempt to bracket $\pm 800\text{mV}$ of the zero current potential. As paint degradation

occurred, it was difficult to determine if the exposed surface was graphite paint or graphite rod, therefore the base supports were changed for later experiments. Data was processed in Microsoft Excel, with linear regression to fit the nearly linear region of the Tafel plot, fixed at +/-200-600mV of the zero current voltage.

To increase visual contrast, electrodes were prepared with copper wire epoxied into ¼" OD PVC tubes to provide electrical contact and graphite paint filling the tube tip to form an isolated electrode surface. It became clear after much testing that this configuration allowed too much copper corrosion current, and the copper oxidation reaction could not be reliably removed from the analysis. Stainless steel 303 rods were also tested as the external electrical contact, however metallic corrosion was still apparent by the location of the zero current voltage in Tafel analysis.

In later experiments, tight control of surface area was exchanged for sure analysis of the graphite paint itself. Electrodes were prepared by painting 0.25in PVC tubes (McMaster-Carr) with graphite paint on the exterior as shown in Figure 3.11.4.



Figure 3.11.4 Graphite paint coated PVC tube electrodes.

The tips were cut to remove stray paint on the tip and/or inside from electrical contact, thereby limiting electroactive surface area to only the exterior surface. Silver filled epoxy (MG Chemicals #8331) was used to attach copper wire leads. Tubes were further trimmed to set the length from contact to tip at 4.25in for the initial test, and

3.5in for all following. The submerged paint surfaces were polished with 400, 600, and 1500 grit sandpaper, successively. The electrodes were mounted in #7 Ace Glass adapters with 1.625in and 0.875 inches protruding from the end of the ground glass fittings, respectively. Given the electrolyte level in aging flasks this was approximately 1.0in and 0.25in of submerged area, respectively. For analysis, each day fresh electrolyte was provided, with 30mL of electrolyte used for consistent wetted area. Tests were run with each of the three halide electrolytes described in 3.3. The electrolytes used for kinetic analysis were the same as those used for aging for each set of aging experiments. Table 3.9.1 summarizes the aging experiment data set conditions.

Table 3.9 Summary of aging experiment conditions

Data Set	Substrate	Electrolyte	Current (mA)	Exposed Area (cm ²)	Analysis Method	Duration (Days)
1	¼" graphite rod, heat shrink	Chloride	1	0.317	Tafel, no purge	53
2	¼" graphite rod, heat shrink	Chloride	1	0.317	Tafel, purged	85
3	PVC tube, 1.0"	Chloride	1.2	5.70	NPV	15
4	PVC tube, 1.0"	Chloride	0	5.70	NPV	15
5	PVC tube, 0.25"	Chloride	1.2	1.27	NPV	23
6	PVC tube, 0.25"	Bromide	1.2	1.27	NPV	37
7	PVC tube, 0.25"	Bromide	0	1.27	NPV	37

Normal pulse voltammetry (NPV) was adopted to generate higher quality Tafel plots. The voltage pulses were applied for 100ms with 15s between samples. The voltage steps were 10mV. The starting voltage was 1.2V vs Ag|AgCl (1.1V for bromide electrolyte) and sequentially larger pulses were applied until 0.8V was reached (0.6V for bromide electrolyte). Between pulses the voltage returns to the starting voltage. The

current is measured at the falling edge of the potential pulse. A script was written to provide a repeatable experimental sequence: purging was applied for 180s, followed by 120s of rest, then open circuit potential was measured until 0.2mV/s voltage stability was reached, or 300s, whichever came first, and finally the NPV test was run. Initially tests were run in triplicate, but an obvious variation in the first data point lead to adopting 4x runs, so that the first data point was thrown out and three data points remained.

The voltage-current plots generated by the NPV script were analyzed in Matlab with the Butler-Volmer fitting script in Appendix A. Oxidation charge transfer coefficient, reduction charge transfer coefficient, equilibrium potential, and exchange current density were used as fit parameters to perform a least squares regression of the data from each test.

4. Modeling and Parameter Fitting

In order to determine the concentration of oxidized chlorine species present in each channel of the discrete voltage profile experiment in Section 3.7, and to accurately measure kinetics as will be discussed in Section 3.9, an electrochemical reactor model was created. The electrochemical model incorporates fluid flow, species diffusion, Butler-Volmer electrochemical kinetics, Nernst potential dependence on species concentration, and bulk dye oxidation kinetics. A diagram is provided in Figure 4.1.

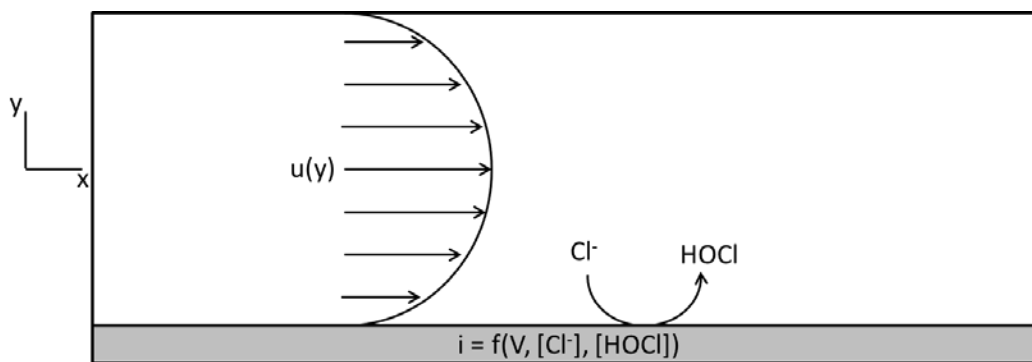


Figure 4.1 Diagram of reactor being modeled.

4.1 The Model

Fluid Flow

The fluid was assumed to be Newtonian, incompressible, and in fully developed laminar flow. Flow is in rectangular channels with width \gg depth such that flow between infinite parallel plates was assumed. The Navier-Stokes Equations in Cartesian coordinates are given in Equation 4.1.1-3.

$$\frac{\partial u}{\partial t} + u \frac{\partial u}{\partial x} + v \frac{\partial u}{\partial y} + w \frac{\partial u}{\partial z} = -\frac{1}{\rho} \frac{\partial p}{\partial x} + \frac{\mu}{\rho} \left(\frac{\partial^2 u}{\partial x^2} + \frac{\partial^2 u}{\partial y^2} + \frac{\partial^2 u}{\partial z^2} \right) + g_x \quad \text{Equation 4.1.1}$$

$$\frac{\partial v}{\partial t} + v \frac{\partial v}{\partial x} + v \frac{\partial v}{\partial y} + w \frac{\partial v}{\partial z} = -\frac{1}{\rho} \frac{\partial p}{\partial y} + \frac{\mu}{\rho} \left(\frac{\partial^2 v}{\partial x^2} + \frac{\partial^2 v}{\partial y^2} + \frac{\partial^2 v}{\partial z^2} \right) + g_y \quad \text{Equation 4.1.2}$$

$$\frac{\partial w}{\partial t} + w \frac{\partial u}{\partial x} + w \frac{\partial v}{\partial y} + w \frac{\partial w}{\partial z} = -\frac{1}{\rho} \frac{\partial p}{\partial z} + \frac{\mu}{\rho} \left(\frac{\partial^2 w}{\partial x^2} + \frac{\partial^2 w}{\partial y^2} + \frac{\partial^2 w}{\partial z^2} \right) + g_z \quad \text{Equation 4.1.3}$$

Conservation of mass gives Equation 4.1.4

$$\frac{\partial u}{\partial x} + \frac{\partial v}{\partial y} + \frac{\partial w}{\partial z} = 0 \quad \text{Equation 4.1.4}$$

Ignoring body forces, the Navier-Stokes equations simplify to Equation 4.1.5

$$\frac{\Delta P}{\mu L} = \frac{\partial^2 u}{\partial y^2} \quad \text{Equation 4.1.5}$$

Here ΔP is the pressure drop across the channel, L is the channel length, μ is the fluid viscosity, and u is the x component of fluid velocity. Boundary conditions are no-slip, i.e., $u = 0$ at $y = \pm H/2$, where H is the channel height and $y = 0$ is the channel centerline.

Mass Transport

Electric field migration was neglected due to supporting electrolyte shielding effects. The steady state mass transport due to fully developed unidirectional convection and diffusion is given by Equation 4.1.6.

$$u \frac{\partial C}{\partial x} = D \left(\frac{\partial^2 C}{\partial x^2} + \frac{\partial^2 C}{\partial y^2} \right) \quad \text{Equation 4.1.6}$$

Here D is the chemical species diffusivity and C is the species concentration. Inlet concentrations are specified, flux at the wall opposite the electrode is assumed to be 0 due to a sufficiently small generation term. At the electrode surface the potential is assumed to be constant and the fluxes normal to the surface are given by Equations 0.4 and 0.5.

Reaction Kinetics

Oxidation kinetics are modeled using the Tafel equation, Equation 4.1.7

$$i = i_0 \left(e^{\frac{\alpha n F}{RT} (V-E)} \right) \quad \text{Equation 4.1.7}$$

The anodic current density at the working electrode is given by i . The convention used is such that a net oxidizing reaction has a positive i value. V is the set voltage, E is the equilibrium potential, F is Faraday's constant, n is the number of electrons transferred in the reaction, R is the gas constant, T is absolute temperature, i_0 is the exchange current density, and α is the charge transfer coefficient. There is no need to involve the concentration dependence in the exchange current density; there is sufficient chlorine in the reduced state that the concentration will be effectively constant. The Tafel equation is chosen because significant overpotential is applied in the reactor to generate measurable products.

The Nernst Equation, Equation 4.1.8, provides the equilibrium potential for a given reaction away from the standard conditions at which reduction potentials are tabulated.

$$E = E^\circ - \frac{RT}{nF} \ln \frac{C_{red}}{C_{ox}} \quad \text{Equation 4.1.8}$$

E° is the reduction potential and standard conditions, C_{ox} and C_{red} are the concentrations of oxidized and reduced species, respectively. Anodic current is converted to oxidized species flux by, j_{ox} , Equation 4.1.9.

$$j_{ox} = \frac{i}{nF} \quad \text{Equation 4.1.9}$$

Combining Equations 4.1.7-9 yields Equation 4.1.10.

$$j_{ox} = \frac{i_0}{nF} e^{\frac{\alpha nF}{RT} \left(V - E^0 + \frac{RT}{nF} \ln \frac{C_{ox}}{C_{red}} \right)}$$
 Equation 4.1.10

Mass conservation yields the reduced species flux, j_{red} , as given in Equation 4.1.11.

$$j_{red} = -\gamma j_{ox}$$
 Equation 4.1.11

Here γ is the ratio of reduced species to oxidized species stoichiometric coefficients. These electrochemical reactions are modeled as surface reactions, with reaction only occurring at the electrode surface. The mass transfer boundary conditions are then given by Equations 4.1.12-13.

$$j_i = -D_i \left. \frac{\partial C_i}{\partial y} \right|_{y=-h/2}$$
 Equation 4.1.12

$$C_i|_{x=0} = C_i|_{y=0} = C_{i,in}$$
 Equation 4.1.13

Only the chloride oxidation to hypochlorite was considered. The standard reduction potential is 1.49V vs NHE. Under the conditions to reach sterilization of about 1ppm hypochlorite, at pH 8 in 35g/L NaCl (seawater conditions) the equilibrium potential is 1.12V vs NHE.

Model Validation

COMSOL Multiphysics was used to build models of both reactor geometries studied. Kinetic parameters were taken from Tafel analysis of aged paint samples. A parametric sweep of voltage was performed, and the results were compared both to experimental results, and a naïve Tafel model with no concentration dependence influencing the equilibrium potential. The results are shown in Figure 4.1.1.

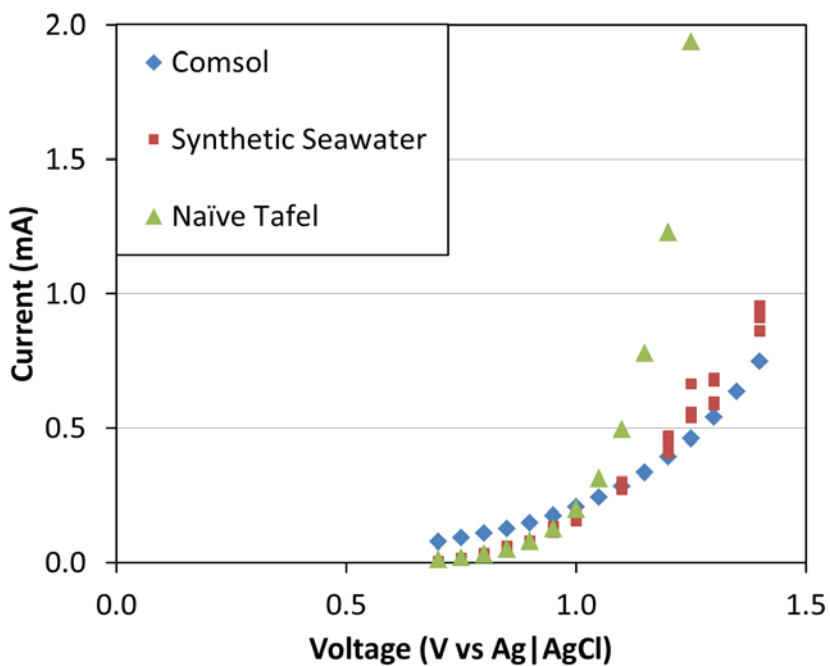


Figure 4.1.1 Comparison of model with experimental results and naïve Tafel kinetic model.

The model is clearly superior to the naïve model for predicting system current at higher overpotentials. Up to 1.05V the naïve model is a better predictor, with the model over-predicting current. With better kinetic data, the model would likely perform far better.

4.2 Reactor Model Characteristics

Studying the reactor model concentration profile with measured kinetic parameters provides insight for future improvements of the modeling and experimental validation. In normal operating conditions, current draw is low and therefore concentration effects are expected to be negligible. Solving the model of a channel from the 9-channel parallel potentiostat experiment shows that the concentration change affects only a very small portion at the reactor surface, as in Figure 4.2.1.

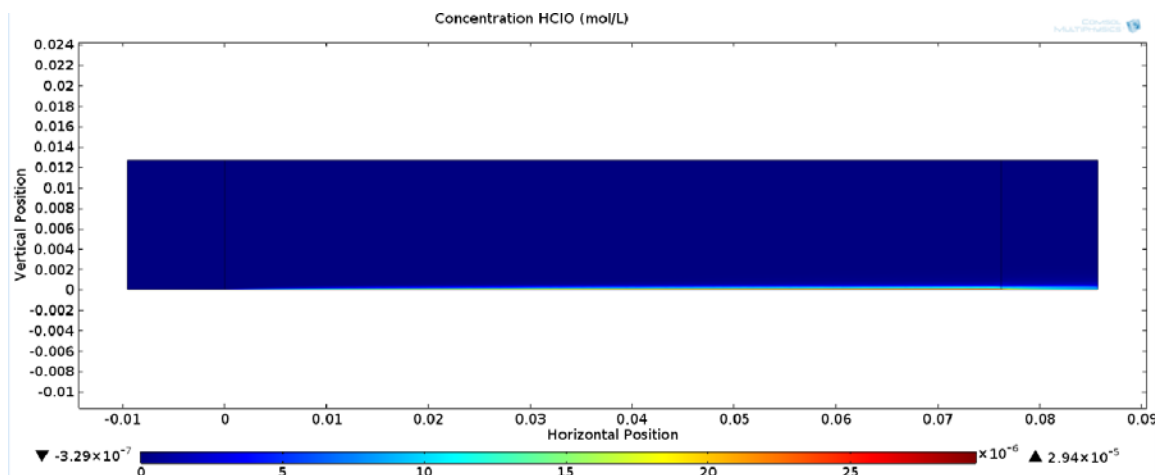


Figure 4.2.1 Concentration of hypochlorite throughout reactor model with device flowrate of 4.0L/min.

Figure 4.2.1 was constructed with the assumption of uniform flux from the electrode surface, which is justified by the small concentration changes. The net current recorded from channel 2, which showed the best performance in the device, was used as the basis for flux. A close-up of the electrode surface near the outlet is given in Figure 4.2.2.

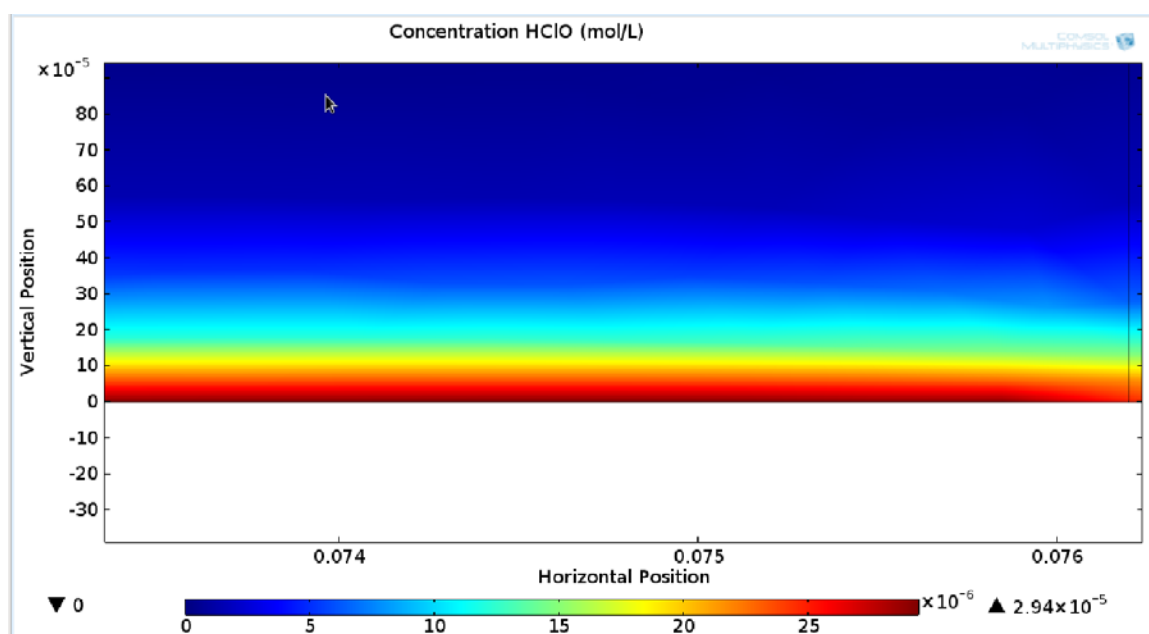


Figure 4.2.2 Close-up view of electrode surface at reactor outlet.

Looking at the concentration at the outlet of the reactor, hypochlorite does not reach more than 600um from the electrode surface. The maximum surface concentration was 29.4μM, or 1.5ppm hypochlorous acid.

5. Results and Discussion

5.1 Paint Development

The mass retention of polyurethane paint was measured to be 49%. On this basis test paints were produced ranging from 45-70% by dry mass graphite. Paints with loading greater than 60% were found to be too thick to get adequate wetting. At the CVP, graphite particles touch and therefore a relatively low resistance path is established. As the loading increases, more graphite-graphite particle contact exists and therefore conductivity is lower, but the change is much smaller than that around the CVP, as demonstrated in Figure 5.1.1.

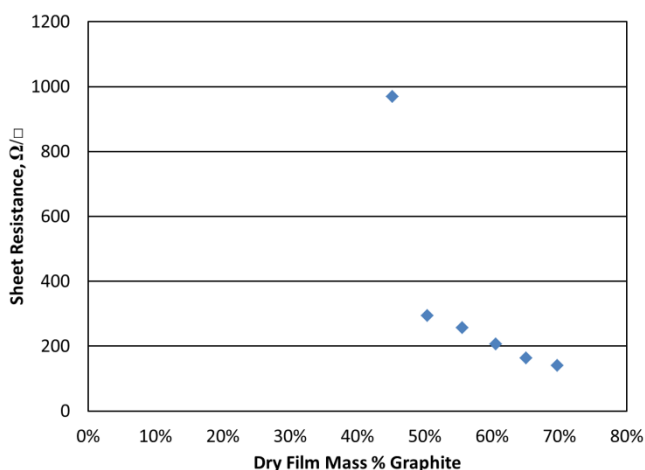


Figure 5.1.1 Sheet resistance as a function of graphite composition. There is a sharp change at the CVP, after which the dependence is much less pronounced.

The CVP was found to be near 45% graphite by dry mass, which leaves 50-60% as the realistic range of paint loading possibilities. A 56% composition was adopted, which was a ratio of 5:8 graphite to wet paint by mass.

The area of an electrode was measured using cyclic voltammetry (CV) paired with the Randles-Sevcik equation. A representative CV scan showing the peak in current due to transition from reaction rate control to diffusion control is given in Figure 5.1.2.

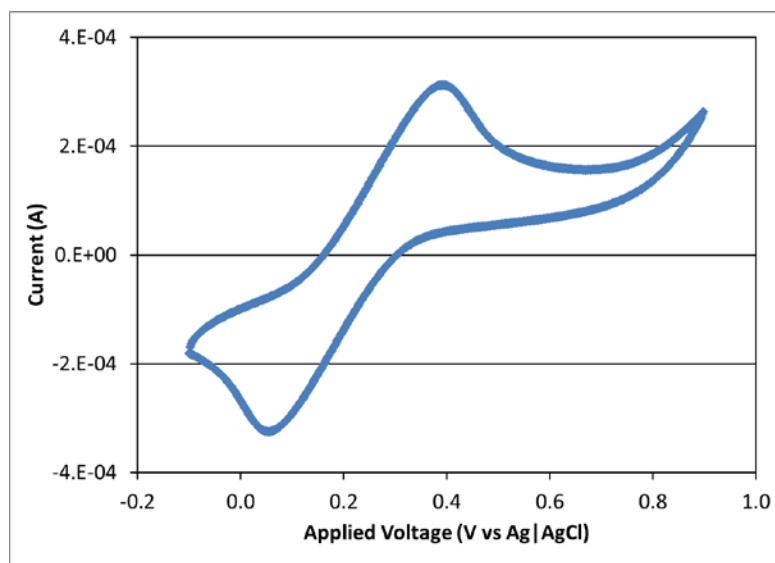


Figure 5.1.2 CV scan of graphite paint electrode on PVC tube base in potassium ferrocyanide electrolyte described in Section 3.3. The counter electrode is a graphite rod, reference is Ag|AgCl, and the scan rate is 20mV/s. The current increases exponentially with applied over-potential, but reaches a peak near 400mV due to mass transport limitations. The faster the scan rate is, the higher the resulting current can reach before becoming mass transport limited. The water splitting reaction is responsible for the increase in current near 800mV.

Regression of the peak current from CV scans as a function of the square root of scan rate yielded the expected linear result as shown in Figure 5.1.3.

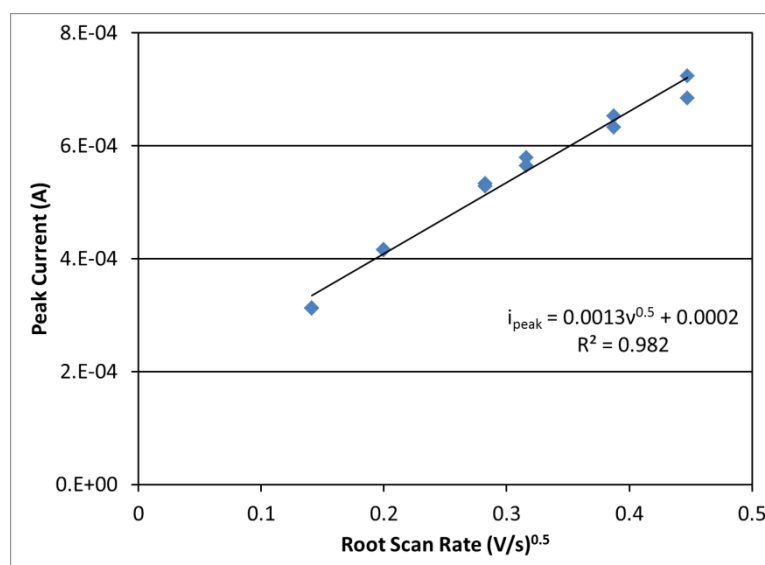


Figure 5.1.3 Dependence of CV peak current on scan rate in potassium ferrocyanide electrolyte. Working electrode was graphite paint on PVC tube, counter was graphite rod, reference was Ag|AgCl. Submerged area of the electrode was 50mm², area calculated from Equation 2.8.8 was 35mm². Discrepancy is most likely due to poor measurement of submerged area and meniscus effects on that measurement. Increasing submerged area to increase confidence in geometric area measurement results in averaging effects which eliminate the current peak.

5.2 Terminal Effect Model

Ocean Sentinel Deployment

The ocean sentinel deployment suffered catastrophic failure due to an unseasonably strong September storm. All data regarding fouling was lost. Data loggers did provide an indication of the potentiostat performance as shown in Figure 5.2.1.

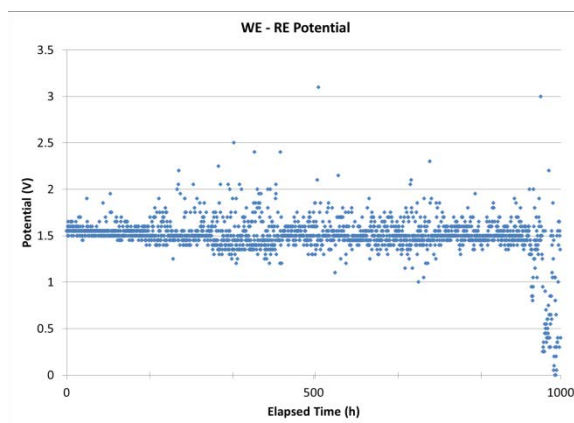


Figure 5.2.1 Potential supplied to working electrode, with reference to Ag|AgCl wire in seawater. The voltage drop indicating detachment of the working electrode coincides with a strong storm event.

The analytical solution developed is poorly suited to solving for kinetic parameters due to strong oscillatory behavior. The model does not fit data well with known charge transfer coefficients and exchange current densities input. Numerical solutions which have been used previously are recommended for continued use.

5.3 Parallel Potentiostatic Flow Cell

The deployment length was 20 days for the parallel potentiostatic flow cell experiment. Data loggers revealed that the battery power supply used was depleted within 8 days. Figure 5.3.1 shows the device upon recovery.

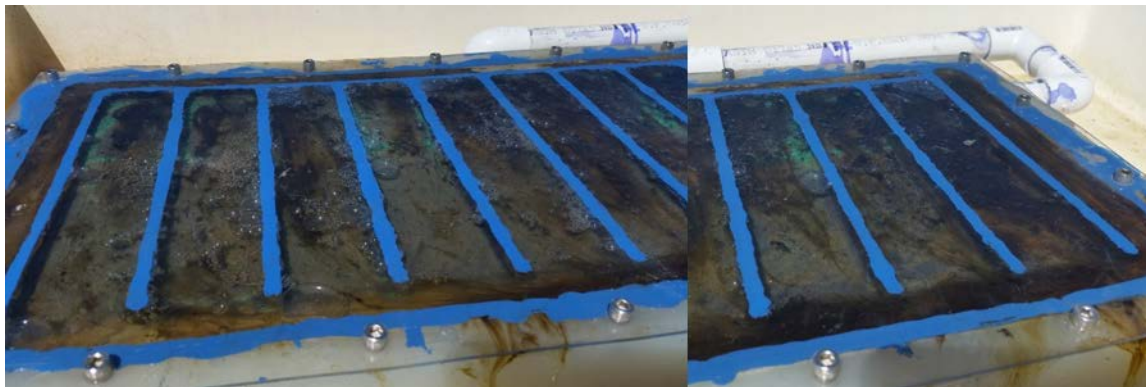


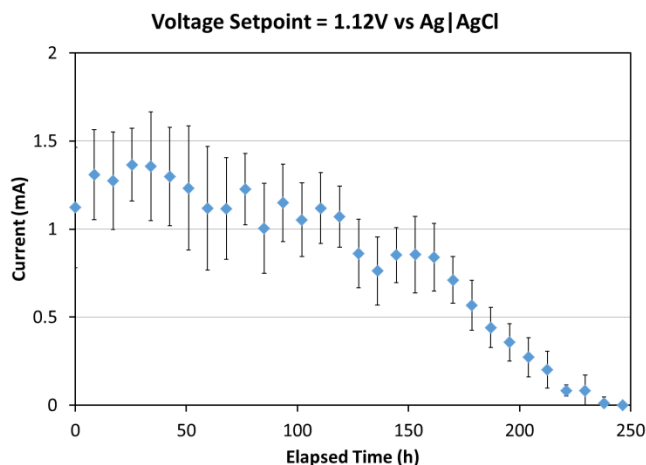
Figure 5.3.1 Device upon retrieval after 20 days in the field. Algae was successfully grown. The control channel is at the far right.

Algal growth hindered flow during the experiment, from an initial value of 4.5L/min to 3.5L/min. In order to purge the loose algae flow was turned to the wide open position. When the lid was removed attached algae was identified from Figure 5.3.2.



Figure 5.3.2 Flow device dried with cover removed. Several channels have clear algae fouling, while all show significant copper oxide development. The counter electrodes remained clear, though film damage is apparent.

Channel 2 showed the least fouling. The set potential was 1.12V vs Ag|AgCl. The operating current over the first week had an average value of 1.1mA with a standard deviation of 0.3mA. The corresponding current density was $28\mu\text{A}/\text{cm}^2$. Based on the modelling results, the surface concentration of hypochlorite was $29.4\mu\text{M}$, or 1.5ppm. The current logged on this channel is shown in Figure 5.3.3.



5.3.3. Current data logger for channel 2. Error bars are one standard deviation, data points are averaged over 8 hour time spans. Raw data taken at 30 minute intervals showed a normal distribution about the mean value over the first 200 samples, with a χ^2 p-value of 0.017. The Durbin-Watson statistic over the same interval was 1.61, which indicates weak autocorrelation. The filtered seawater supply also feeds many other locations at the HMSC site which likely caused periodic variability in the flow rate. Electrodes were isothermal, but control electronics may have been affected by daily temperature fluctuations.

5.4 Non-Graphitic Materials

Titanium nitride paints proved to require much larger mass loadings to achieve conductivity than graphite powder, probably due to density effects. Even at 70% mass loading, conductivity was too low to be useful. Based on the high loading needed and cost considerations, TiN does not appear to be a reasonable option.

Within the two week test timeframe, all ITO coated PET panels had been completely stripped of ITO. The loss of characteristic film tint was apparent and sheet resistance measurements confirmed the lack of conductivity. This was unexpected due to the low solubility of SnO_2 on which ITO is based. Both ITO plates became separated from the silver epoxy bond, where it appeared that the silver had oxidized. Retrospectively the potential used was a bit extreme, and this work should be revisited. Test panel results are given in Figure 5.4.1.

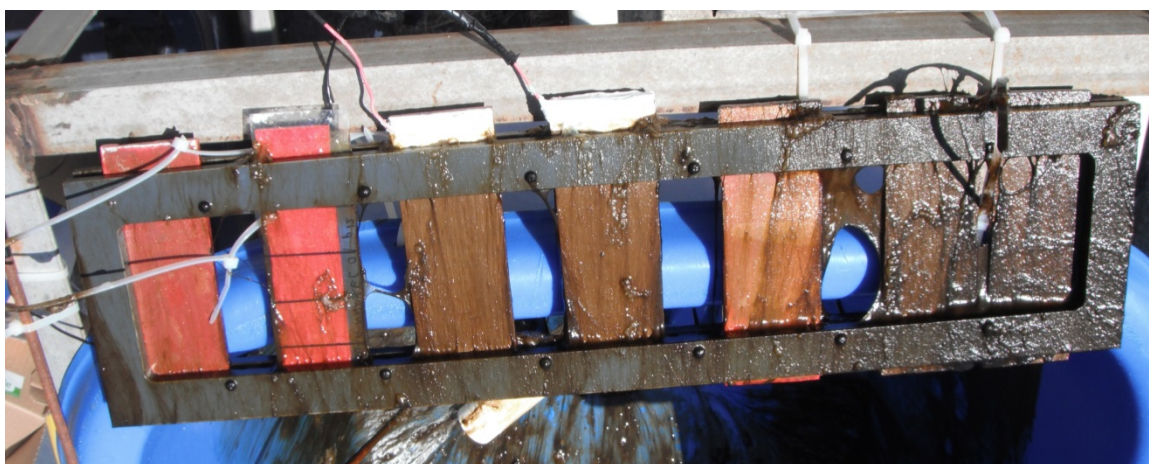


Figure 5.4.1 TiN and ITO coatings recovered after six days in filtered seawater tank at Hatfield Marine Science Center. From left to right: ITO, ITO, TiN epoxy, TiN polyurethane, ITO, TiN epoxy, TiN polyurethane.

5.5 Electrochemical Reactor Results

An electrochemical microreactor was fabricated with graphite paint electrode surfaces, giving well defined hydrodynamic conditions for electrochemical kinetic analyses. The data collected using this reactor and the determined kinetic parameters are presented here.

Oxygen Evolution Background

Because of the background oxygen evolution reaction, blank experiments were run with potassium nitrate electrolyte to measure the kinetics of that reaction. Results of these experiments are given in Figure 5.5.1.

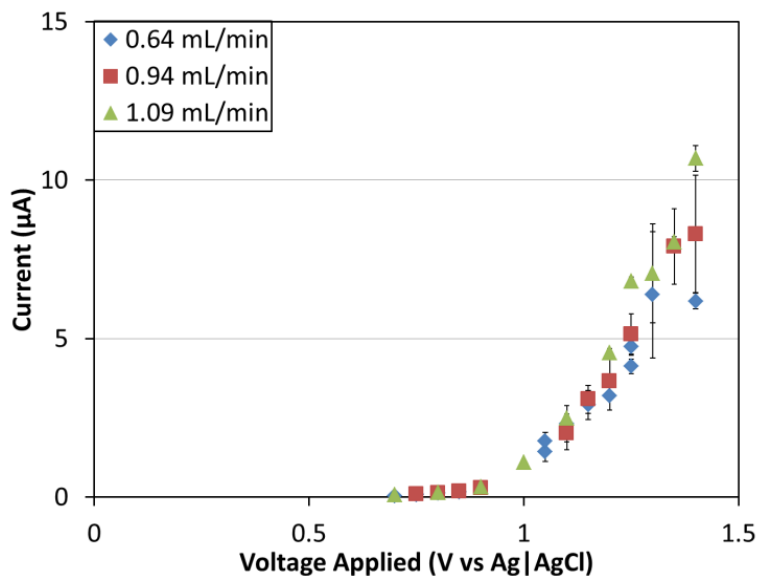


Figure 5.5.1 Current-voltage plot from electrochemical reactor fed with non-reactive supporting electrolyte. Error bars are 1 standard deviation. Bubble formation affecting electrode surface area causes increased current variability at high overpotentials.

Data from 3 flow rates is shown. There appears to be no dependence on flowrate, which suggests that water electrolysis was occurring. While the applied potential is lower than the expected requirement for this reaction, degassing the electrolyte reduced the equilibrium potential and consequently increased the actual applied overpotential. Nitrate anions are known graphite intercalants, however, and nitrate intercalation into oxidized graphite is a possible reaction given the system. Graphite lattice structure change has been demonstrated due to nitrate intercalation at 1.5V vs sodium saturated calomel electrode in 1M HNO₃ [76]. This potential is above the maximum potential applied in this work, making the likelihood of this reaction occurring small. Blue 1 dye was used as an indicator of hypochlorite generation in addition to reaction current. The reactor was run with potassium nitrate supporting electrolyte and dye to determine if the dye was electrochemically active. The results are shown in Figure 5.5.2.

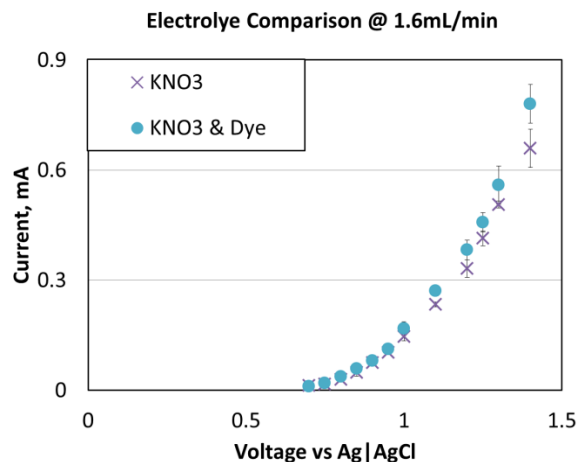


Figure 5.5.2 Current-voltage plot from electrochemical reactor fed with non-reactive KNO_3 supporting electrolyte, with and without blue 1 dye $3.88\mu\text{M}$. Error bars are given at 1 standard deviation. It appears that the dye is directly oxidized in the electrochemical cell.

As a second check on dye degradation, the absorbance was also observed. As expected neat KNO_3 electrolyte showed no absorption peaks. The same electrolyte with $3.88\mu\text{M}$ blue 1 showed clear absorption signal. The results of these tests are given in Figure 5.5.3.

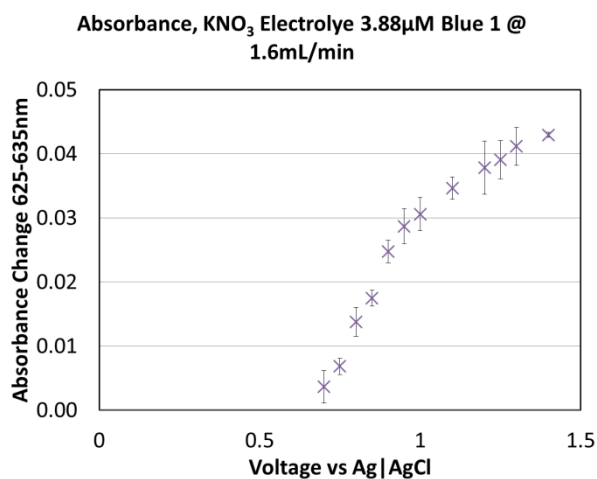


Figure 5.5.3. Absorption signal clearly indicates bleaching activity. Reaction could either be direct oxidation of the dye or bleaching due to hydrogen peroxide generation.

To differentiate between direct oxidation of blue 1 dye and hydrogen peroxide bleaching of the dye, the cell was run with non-reactive KNO_3 electrolyte only at 1.4V vs Ag|AgCl. The effluent was mixed with concentrated dye solution to make $3.88\mu\text{M}$ and the 630nm absorption peak was observed as a batch reaction in a 1cm polystyrene cuvette. The absorption did not show evidence of bleaching, suggesting that dye is oxidized at the anode during operation.

Chloride Electrolyte

Chloride electrolyte was run through the electrochemical reactor to obtain data with which to fit model parameters. As shown in Figure 5.5.1, significantly more current is drawn for a given potential with chloride electrolyte than with KNO_3 electrolyte.

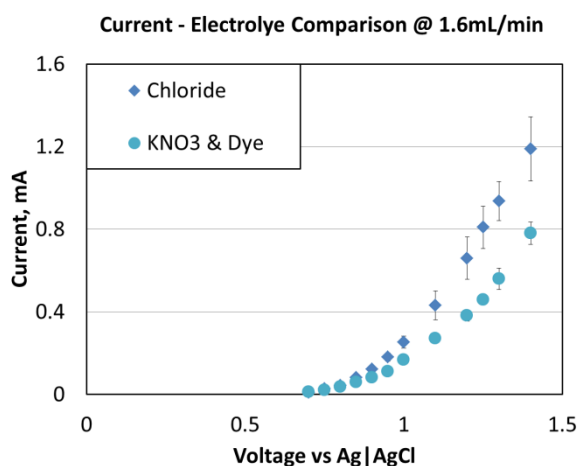
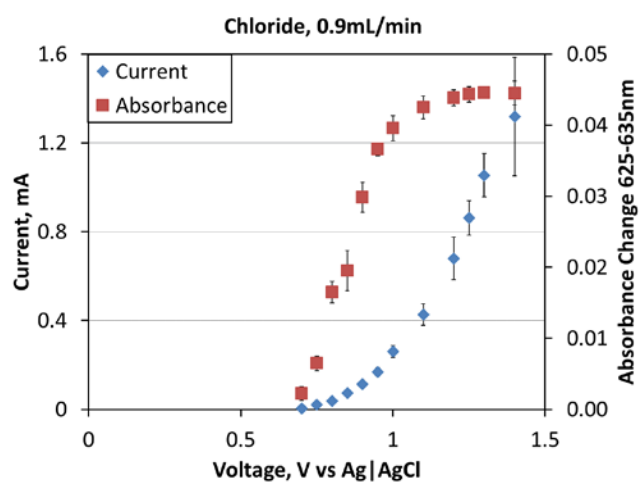
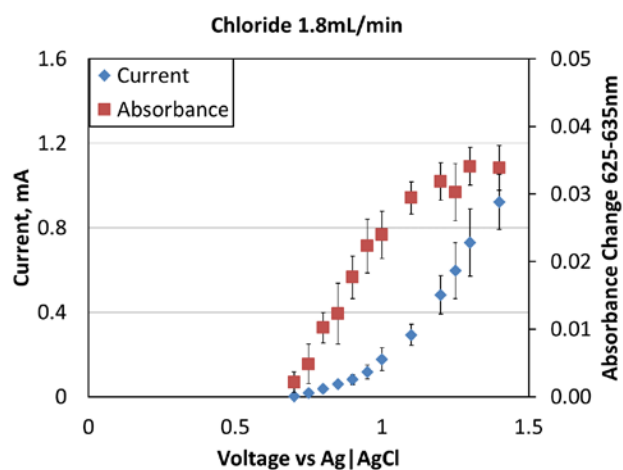


Figure 5.5.4 Current draw difference between chloride and KNO_3 electrolytes with blue 1 dye. Error bars are one standard deviation.

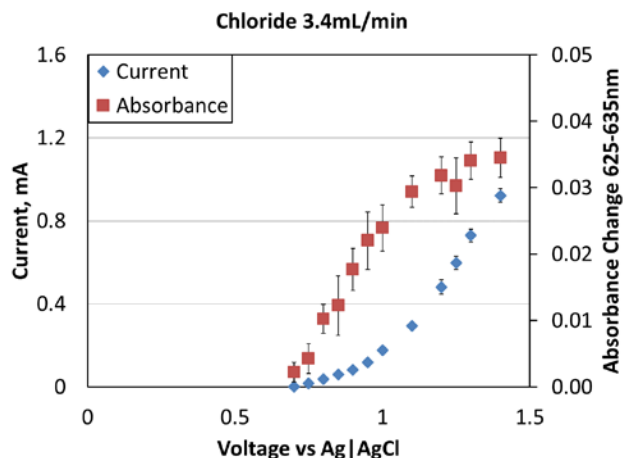
The current – absorbance relationship is given for chloride electrolytes in Figures 5.5.5-7.



5.5.5 Chloride electrolyte current and absorbance comparison at flow rate of 0.9mL/minute. Error bars are one standard deviation.



5.5.6 Chloride electrolyte current and absorbance comparison at flow rate of 1.8mL/minute. Error bars are one standard deviation.



5.5.7 Chloride electrolyte current and absorbance comparison at flow rate of 3.4mL/minute. Error bars are one standard deviation.

At each flow rate the absorbance signal shows a sharp increase at lower potential and begins tapering off at higher potential, while the current displays exponential growth. This is an indication that dye is being oxidized in the reactor at a lower potential than chloride and reaching the mass transport limitation while the much larger chloride oxidation current continues to grow as expected.

The dependence of reactor current upon flow rate is shown in Figure 5.5.8.

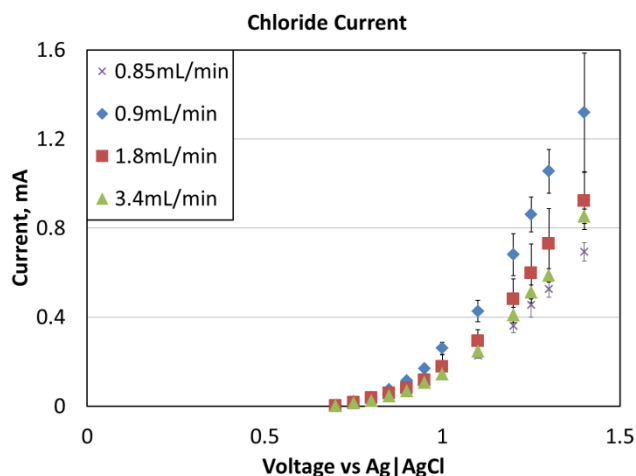


Figure 5.5.8 Current dependence on voltage, variation with flow rate in chloride electrolyte. Error bars are one standard deviation.

Initial tests showed a decreasing trend in reactor current with increasing flow. Further investigation shows that this was likely a conditioning effect, as the high-value series was the first run. The current voltage relationship is exponential as expected, with increasing current draw for increasing flow rates. Comparison of the absorbance signals is given in Figure 5.5.9.

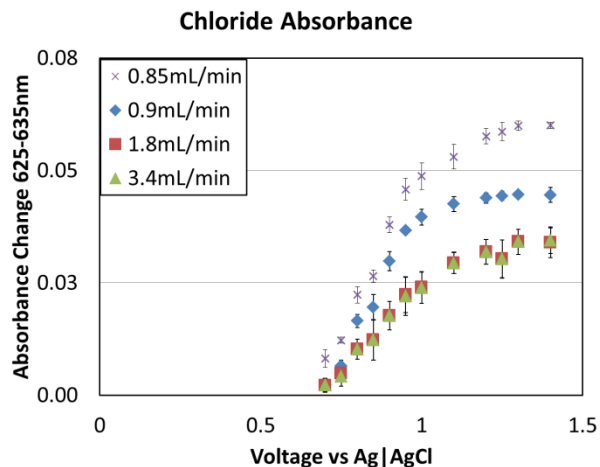


Figure 5.5.9 Absorbance signal as function of voltage at four flow rates. The value at 0.9mL/min was taken before the degassing unit was utilized between the reactor outlet and detector.

The higher absorbance signal is expected due to the extended residence time. At high flow rates the absorbance signals are indistinguishable.

Bromide Electrolyte

Bromide is a potentially relevant species in electrochemical systems in seawater. Even at low concentration, the more labile bromide may account for a significant portion of the reaction current. The current-voltage plots for bromide and chloride electrolyte are compared in Figure 5.5.10.

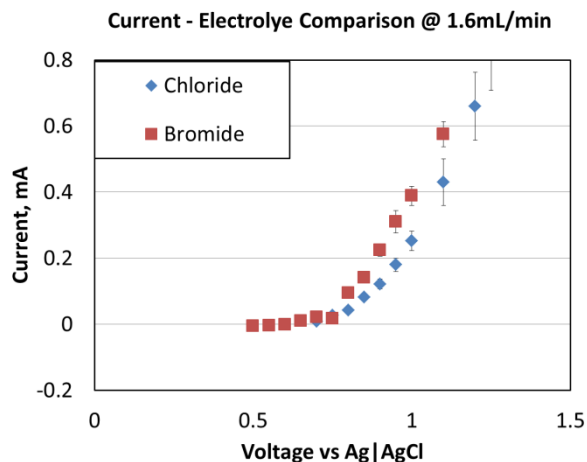


Figure 5.5.10 Current comparison of chloride and bromide electrolytes at 1.6mL/min flow rate. Error bars are one standard deviation.

The molar concentration of bromide is half that of chloride, and yet the current is much larger due to the lower reduction potential. Comparison of the absorbance signals from these two conditions shows a more drastic difference, as shown in Figure 5.5.11.

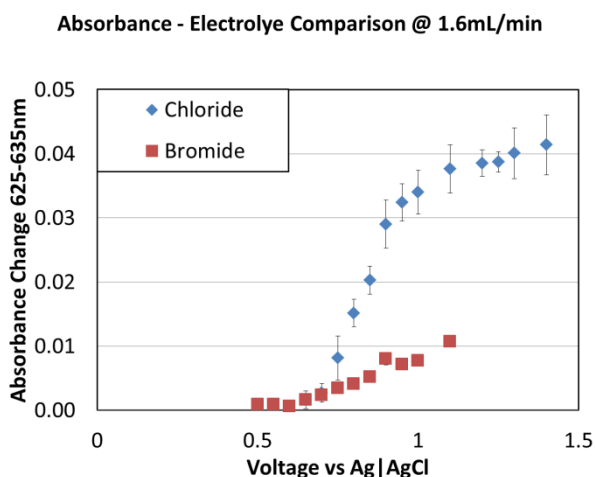


Figure 5.5.11 Absorbance comparison of chloride vs bromide electrolytes.

The reduced absorbance of the bromide electrolyte plot is counter-intuitive when considering the greater current. To understand what is happening the current absorbance curve for bromide is examined in Figure 5.5.12.

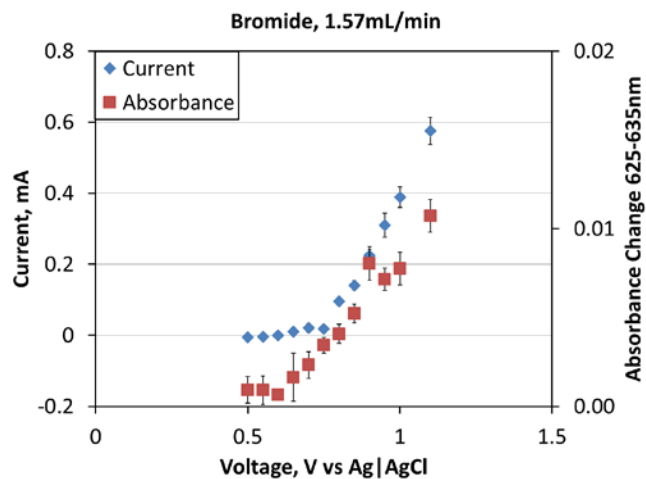


Figure 5.5.12 Current and absorbance as functions of voltage for bromide electrolyte.

The absorbance signal clearly begins to increase at lower potential than the current. This suggests that the blue 1 reduction potential is lower than the bromine reduction potential in this system. When bromide oxidation begins to be driven, the much larger concentration of bromine washes out any significance that blue 1 may have contributed to the current. The absorbance signal in bromide electrolyte is likely due to oxidized dye oxidizing bromine and restoring the chromophore.

Model Seawater

The absorbance signal of synthetic seawater as a function of voltage is compared for that of chloride electrolyte in Figure 5.5.13.

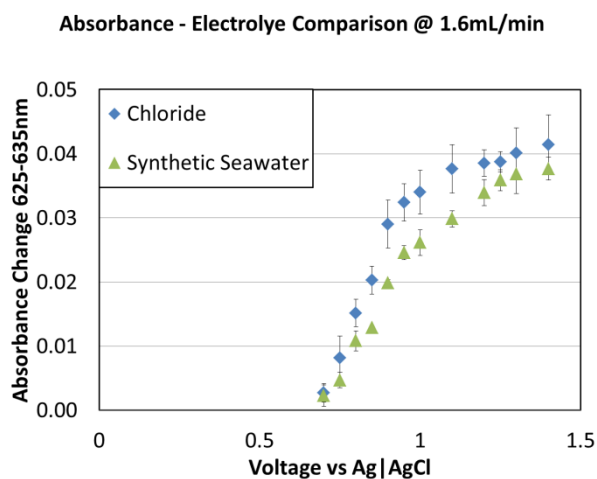


Figure 5.5.13 Absorbance-voltage curves for chloride electrolyte and synthetic seawater.

The absorbance signal is surprisingly lower for synthetic seawater than for chloride electrolyte. The current of synthetic seawater as a function of voltage is compared for that of chloride electrolyte in Figure 5.5.14.

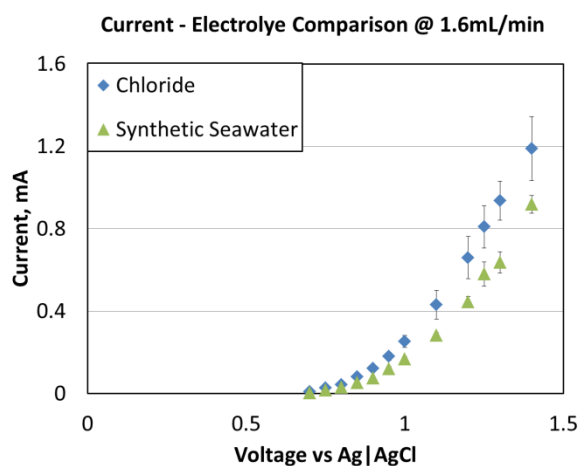


Figure 5.5.14 Current-voltage curves for chloride electrolyte and synthetic seawater.

The current generated when running synthetic seawater through the reactor was also lower than that with chloride electrolyte. This explains the lower absorption signal. Because the bromide electrolyte generated more current, this is not likely a trend due to electrolyte composition, but rather a function of error and electrode conditioning.

5.6 Degradation Studies

Graphite Paint on Graphite Rods, Chloride Electrolyte

Graphite rods coated with 65 weight percent graphite filled paint and sealed with heat shrink to isolate the tips were aged in electrolyte galvanostatically. The current density was restricted by bubble formation arising from gas evolving reactions. The exchange current density of chloride oxidation at these electrodes is given in Figure 5.6.1.

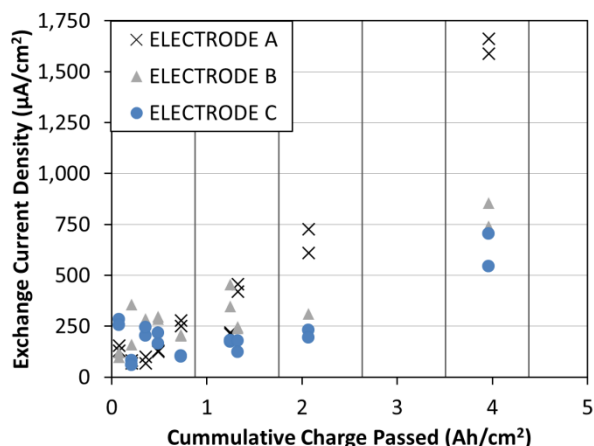


Figure 5.6.1 Observed changes in exchange current density as a function of cumulative current experienced by three independent electrodes. A cumulative charge of $4\text{Ah}/\text{cm}^2$ is the equivalent current experienced by an electrode over a period of 22.5 years. The increase in exchange current density in all three electrodes was unexpected, but indicates increasing performance with use. Vertical lines represent increments of 5 years of service life at $20\mu\text{A}/\text{cm}^2$.

The variation between electrodes was large, because these electrodes were not polished, leaving significant variation in active area. Normalizing the exchange current density of each electrode to the initial measured value accounts for these variations, and the trend is shown in Figure 5.6.2.

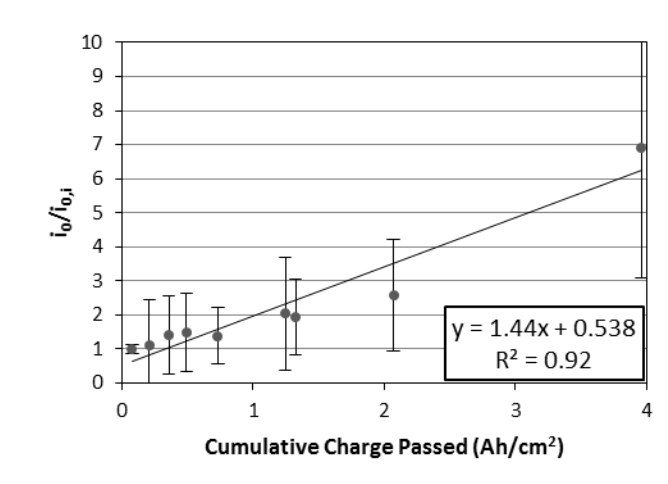


Figure 5.6.2 Exchange current density normalized to initial values. Points indicate average of 2 scans run on each of 3 electrodes for a given state of aging. Error bars are one standard deviation. Exchange current density showed a definitive increase with aging.

Performing a Student's t-test on the null hypothesis that variation is due to noise rather than a true evolution of the exchange current parameter gives a minimum t score of 5.3 between the 3 electrode tests. This is sufficient to reject the null hypothesis with less than 5% chance of a false negative. The charge transfer coefficients for the same set of experiments are given in Figure 5.6.3.

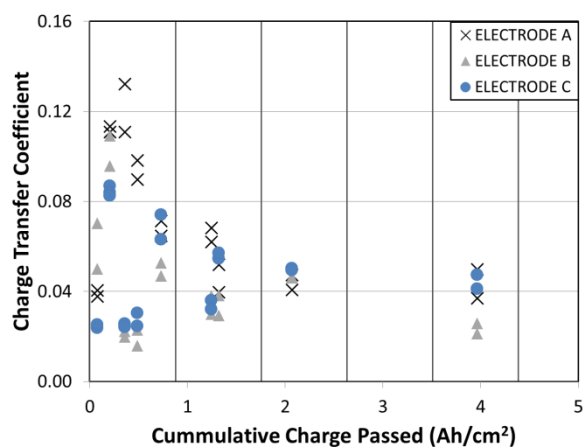


Figure 5.6.3 Charge transfer coefficient variation with aging. Vertical lines indicate increments equivalent to 5 years of service life. The charge transfer coefficient for this

system is low, but the large exchange current density and low operating current make it acceptable.

The charge transfer coefficients show a significant amount of variation early on. It is likely that graphite terminal groups' oxidation state played a role in this early variance. The t-scores for two of the three electrodes accept the null hypothesis that there is no trend at the 95% confidence level; however the third electrode calls for rejection of that hypothesis. The charge transfer coefficients normalized for each electrode are given in Figure 5.6.4.

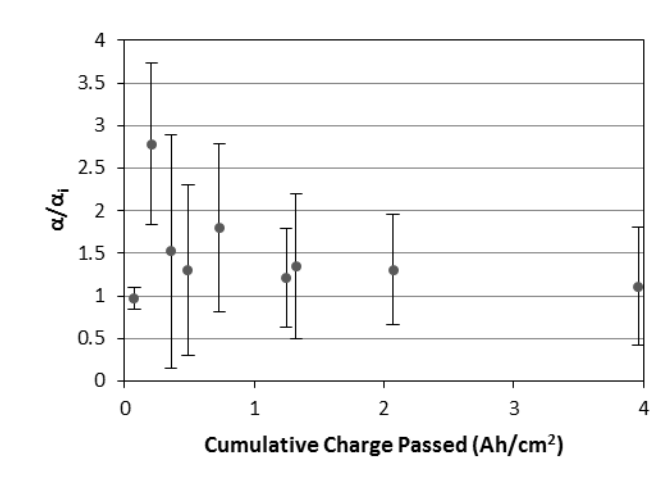


Figure 5.6.4 Charge transfer coefficient normalized to initial values. Points indicate average of samples measured at a given state of aging. Error bars are one standard deviation. Any trend observed is likely due to noise.

Unlike exchange current density, the charge transfer coefficients should be the same between electrodes due to identical preparations. One source of variation was suspected to be the subjective choice of over-potential range to use as the assumed linear region. The previous data was processed using linear regression of the portions of the curves ± 0.200 to 0.600 V from the 0-current potential. Further processing used a least squares solution comparing the Butler-Volmer kinetic model with the observed i-V trend for the whole curve. The fit parameters were exchange current density, anodic

charge transfer coefficient, cathodic charge transfer coefficient, and equilibrium potential. The result of the fitting is given in Figure 5.6.5.

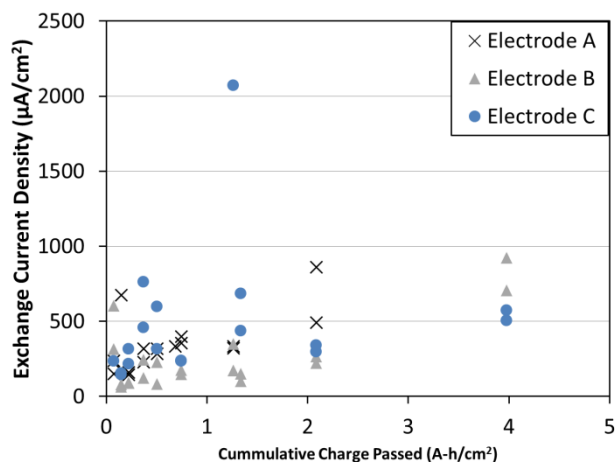


Figure 5.6.5 Exchange current density as function of aging. Values are determined with a least squares fit to the Butler Volmer Model.

The least squares fit provides similar results, however some data points returned non-physical results, such as negative exchange current density or charge transfer coefficients larger than 1. These anomalies provided objective criteria for discarding data points. Upon discarding the data points that yielded non-physical results, the values of normalized exchange current density, oxidation charge transfer coefficient, and reduction charge transfer coefficient were lumped together for all scans of all 3 electrodes. A t-test of the significance of the slope only showed significance for the reduction charge transfer coefficient, which had a slope of $0.119 \pm 0.032 (\text{A}\cdot\text{h})^{-1}$ at the 95% confidence level. This is heavily influenced by a high-value measurement as shown in Figure 5.6.6.

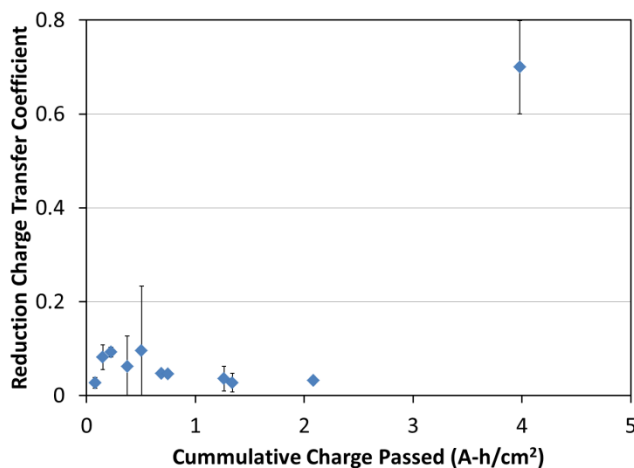


Figure 5.6.6. Reduction charge transfer coefficient as function of aging for graphite filled polyurethane paints on graphite rods in chloride electrolyte. Error bars are one standard deviation.

The previous results were found with the initial method of Tafel analysis: sweeping from lower to higher potential at 20mV/s in a staircase ramp in un-purged electrolyte. To generate cleaner results the electrolyte was purged with N₂ prior to analysis to eliminate the possibility of oxygen reduction interference. The magnitude of the exchange current density remained similar as given in Figure 5.6.7.

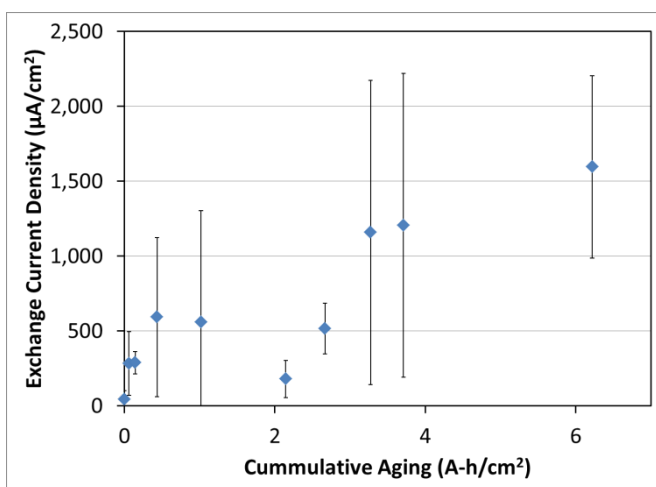


Figure 5.6.7 Exchange current density as function of aging for second set of 3 electrodes. Tafel scans taken in purged electrolyte.

The charge transfer coefficient values for the oxidation and reduction reactions are also similar as shown in Figure 5.6.8.

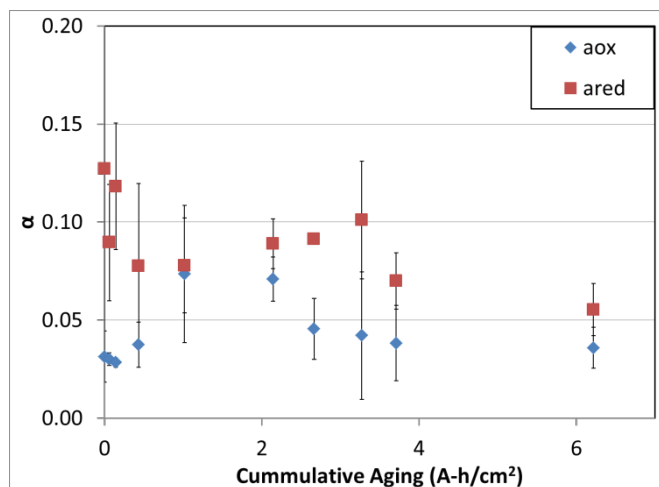


Figure 5.6..8 Charge transfer coefficient as function of aging for second set of three electrodes, Tafel scans taken in purged electrolyte.

In this repeat of the experiment, the charge transfer coefficients again showed no statistically significant trend at the 95% confidence level. The exchange current density did, however, show a significant trend with slope of $40 \pm 32 \text{ (A-h)}^{-1}$.

One of the three electrodes suffered clear separation of paint from the graphite rode at about 3Ah/cm^2 , therefore the last two points are taken with only the remaining two electrodes. Due to blistering as in Figure 5.6.9 and the similarity in appearance of graphite paint and graphite rods, the validity of analysis reflecting graphite paint kinetics rather than graphite rod kinetics was a concern. This called for evolution of the electrode samples.



Figure 5.6.9 Graphite paint on graphite rod samples after aging in chloride electrolyte. Blistering did appear to be a problem.

Graphite Paint on PVC tubes, Chloride Electrolyte

To create electrodes which guaranteed analysis of only graphite paint electrocatalysis, graphite paint electrodes were prepared by coating PVC tubes with graphite filled paint. The form factor is not ideal for control of surface area, as exposed area is sensitive to evaporation and meniscus effects. To minimize relative change in area, significantly more surface area was exposed than with paint tip electrodes on the end of $\frac{1}{4}$ " rods. Hardware limitation on current output paired with increased area limited the current density achievable. A new analysis method was also developed which applied periodic, ramped voltage pulses rather than a staircase ramp. The resulting data showed much better consistency as shown by the exchange current densities measured in Figure 5.6.10.

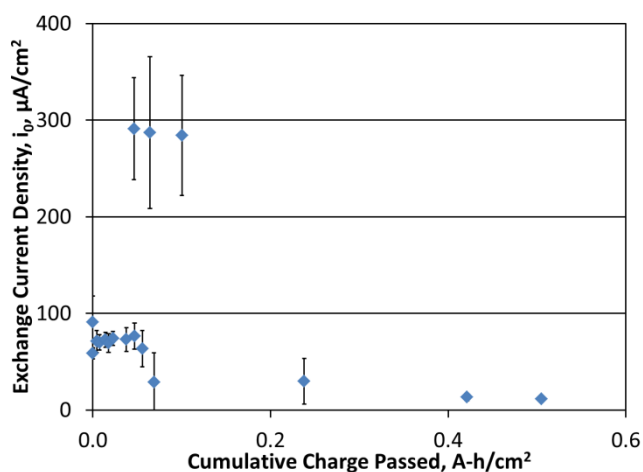


Figure 5.6.10 Exchange current density of graphite paint on PVC rods measured with pulsed voltammetry method as function of galvanostatic aging in chloride electrolyte.

Each point is the average of three different electrodes, each of which was run 3 or 4 times with the first point discarded. The error bars are one standard deviation.

Two data sets are combined here, one with electrodes submerged 1" into electrolyte for consistent area measurements, the other submerged ¼" for faster aging. The points at 290 $\mu\text{A}/\text{cm}^2$ with large error are for electrodes submerged ¼" in electrolyte for faster aging. The measured values are lower, however much more consistent with the newer method compared with the graphite rod substrate. The normalized charge transfer coefficient plot, Figure 5.6.11 shows less change, however the slope of the line in this analysis was negative rather than positive.

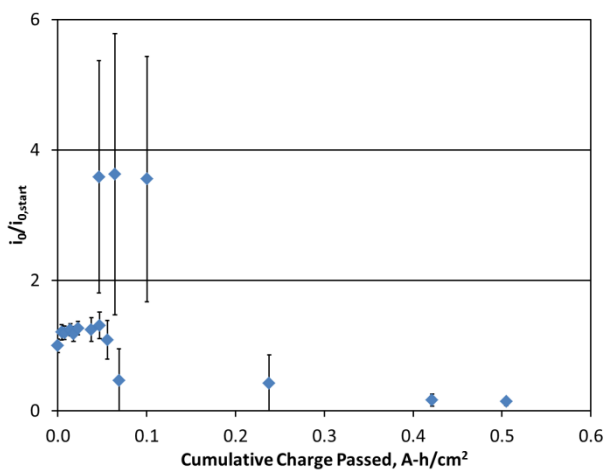


Figure 5.6.11 Normalized exchange current density with aging in chloride electrolyte.

Applying linear regression, the p-value of the slope is 7.5E-5, indicating that it is important. The slope is $-3.0 \pm 1.4 \text{ (A-h)}^{-1}$ at the 95% confidence level. The decreasing trend of this data is more trustworthy than the results of paint tips on graphite rods, because there is no possibility of a graphite rod providing electrocatalytic area. The charge transfer coefficient again did not show a statistically significant trend with aging, the data for these experiments is given in Figure 5.6.12.

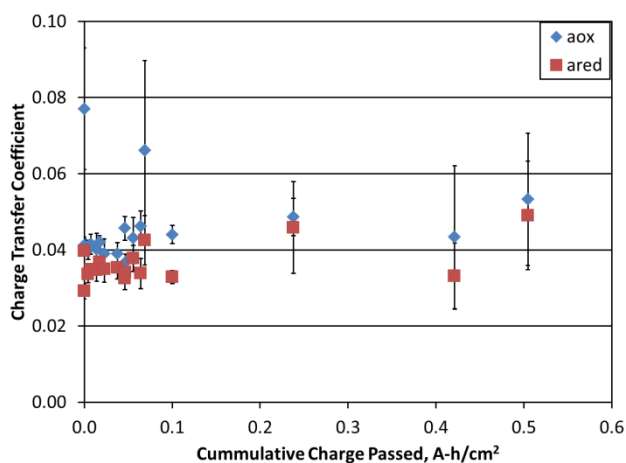


Figure 5.6.12 Charge transfer coefficient with aging in chloride electrolyte.

To determine if any changes observed were due to current flow, or conversely, if any changes were prevented by current flow, blank experiments were run identical to the aging experiments, less the galvanostatic aging. The electrodes compared were submerged 1" in chloride electrolyte. Statistical handling of the data shows that the null hypothesis of no slope in the data only need be rejected for the reduction charge transfer coefficient, which showed a slope of $2.1E-4 \pm 1.2E-4 \text{ day}^{-1}$. Comparison of oxidation and reduction charge transfer coefficients between aged and unaged runs is given in Figures 5.6.13 and 14, respectively.

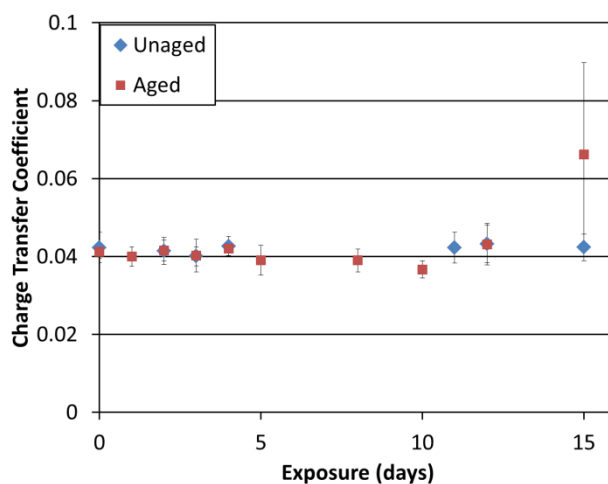


Figure 5.6.13 Charge transfer coefficient for oxidation reaction on graphite paint electrode, comparison of aged and unaged electrodes.

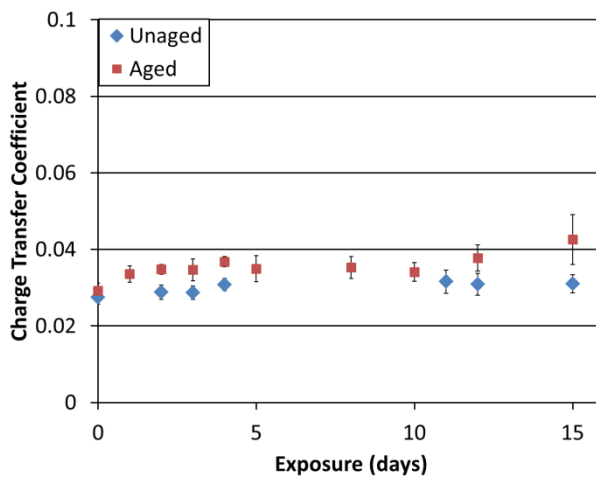


Figure 5.6.14 Comparison of reduction charge transfer coefficient with exposure time in chloride electrolyte. The unaged electrode had no current or voltage applied, the aged electrode was subjected to $211\mu\text{A}/\text{cm}^2$.

Comparison of the aged and unaged exchange current densities is shown in Figure 5.6.15.

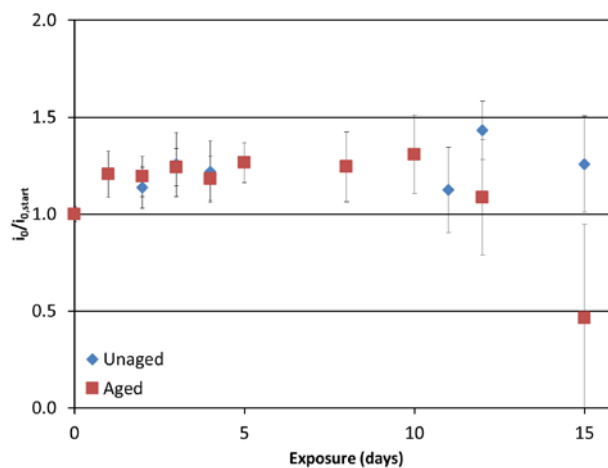


Figure 5.6.15 Comparison of exchange current density with exposure time in chloride electrolyte. The unaged electrode had no current or voltage applied, the aged electrode was subjected to $211\mu\text{A}/\text{cm}^2$.

Graphite Paint on PVC tubes, Bromide Electrolyte

Bromide is a minor constituent in seawater, yet understanding how it affects the graphite paint electrocatalysis is important to identify. Analogous aging studies were conducted with bromide electrolyte, with graphite paint coated PCV rods submerged $\frac{1}{4}$ " in bromide electrolyte and subjected to 1.2mA or no current. Comparison of the aged and unaged electrode oxidation charge transfer coefficients and normalized exchange current densities are given in Figures 5.6.16 and 17, respectively.

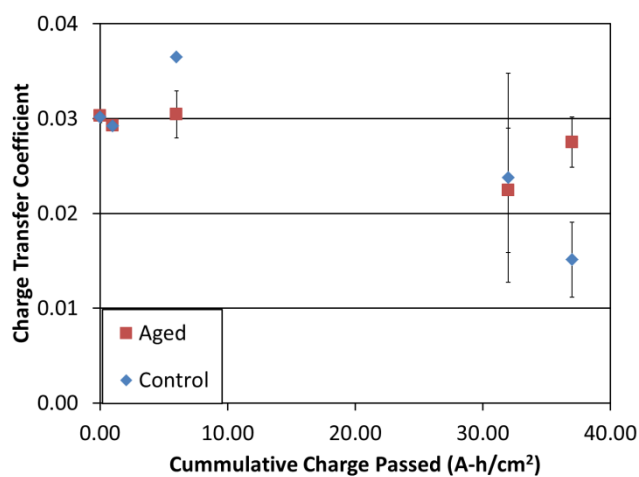


Figure 5.6.16 Aged and control electrode charge transfer coefficient.

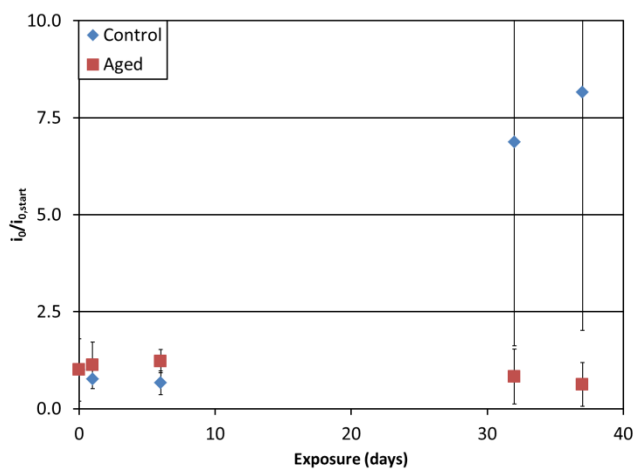


Figure 5.6.17 Aged and control electrode exchange current density.

It is worth noting that the last points with high variance used the Butler-Volmer routine, while due to insufficient negative current in the Tafel scans, the early points were fit to the Tafel kinetic model. There were statistically significant trends in the aged oxidation charge transfer coefficient and the unaged exchange current density, of $-9.5 \times 10^{-3} \pm 4.6 \times 10^{-3} (\text{A-h})^{-1}$ and $1.74 \times 10^{-5} \pm 9.9 \times 10^{-6} \text{day}^{-1}$, respectively, at the 95% CL. The charge transfer coefficient as a function of charge passed is given in Figure 5.6.18.

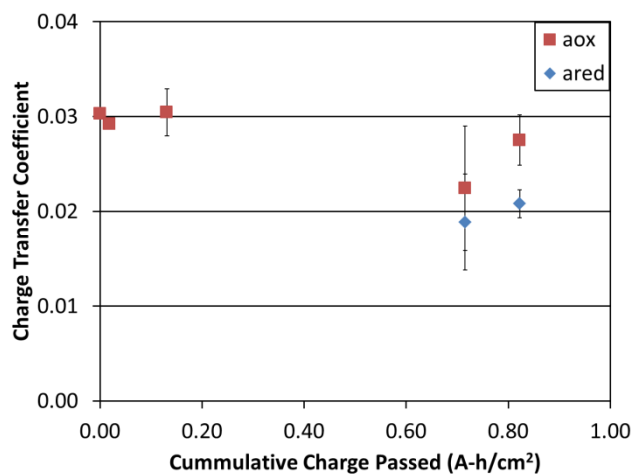


Figure 5.6.18 Charge transfer coefficient as a function of galvanostatic aging.

The exchange current density was much lower for bromide than chloride electrolyte.

The exchange current density trend is given in Figure 5.6.19.

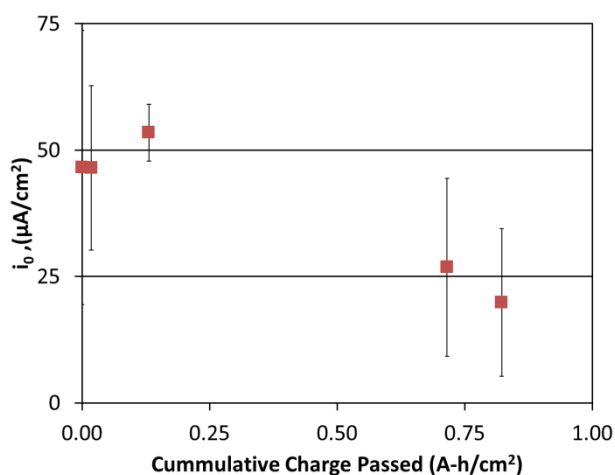


Figure 5.6.19 Exchange current density as a function of galvanostatic aging.

Looking at the normalized values in Figure 5.6.20 there appears to be a negative trend, however the p-value for the slope is only 0.27.

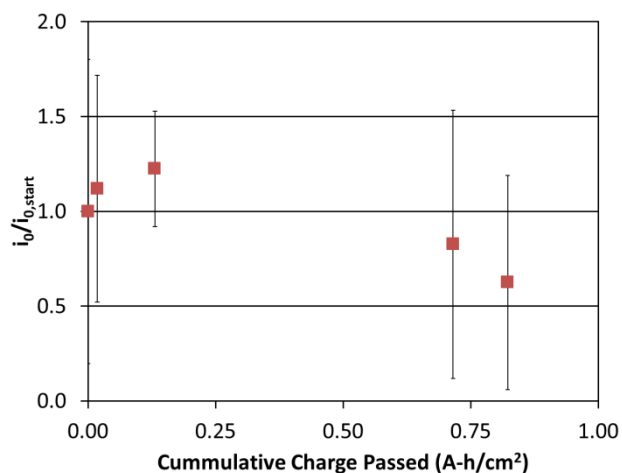


Figure 5.6.20 Normalized exchange current density as a function of galvanostatic aging.

Further work should examine electrode mass loss, as the electrode in Figure 5.6.21 clearly shows a physical after aging in bromide electrolyte.



Figure 5.6.21 Electrode after anodic aging at $211\mu\text{A}/\text{cm}^2$ in bromide electrolyte, showing some clear physical change.

6. Conclusion

Graphite-polyurethane paints have been found to be suitable for use in antifouling applications in the range of 50-60% graphite by mass. Higher loadings have clumping issues and poor coating characteristics, for little gain in conductivity. Below 50% the film resistance is excessive. Graphite paint electrodes were deployed in several trials. While some complications were encountered with many field experiments, the methods have been developed and the groundwork is laid for future work. Non-graphitic conductive thin films have been tested as well. Titanium nitride was not an ideal conductive pigment due to density issues, both settling in paint films and high mass loading requirements. Indium tin oxide stripped entirely off of PET plastic when held at potential in seawater tank experiments.

Micro-scale electrochemical reactors were designed and fabricated to test reaction kinetic models. Reaction current as a function of voltage has been measured for non-reactive potassium nitrate electrolyte, chloride electrolyte, bromide electrolyte, and synthetic seawater, all buffered to pH=8 with tris(hydroxymethyl)aminomethane. Water splitting and/or peroxide generation at anodic conditions showed no dependence on flow rate, which was expected. Chloride electrolyte was run as the base study, because chloride oxidation is the likely primary mechanism of antifouling efficacy. The variation in current draw from one condition to the next was exceeded by the variation due to uncontrolled factors and conditioning. The curves all followed a generally exponential trend, representative of the Tafel kinetic regime and indicative that concentration effects may be negligible. Blue food dye FD&C #1 was used as an indicator of generation of bleaching compounds. The absorbance change at the 630nm peak for blue 1 dye in potassium nitrate and chloride electrolytes was very similar, indicating that direct oxidation of dye occurs or water is oxidized to something like hydrogen peroxide. Bromide oxidation showed more current draw than the other tests, however the absorbance change was significantly smaller, indicating that bromide and/or bromine somehow interfere with the dye oxidation reaction. Synthetic seawater current draw was not significantly different from plain chloride electrolyte.

Graphite paint electrode kinetics were also studied with more traditional Tafel plot methods, and kinetic parameters were correlated with cumulative charge passed through the system. For chloride oxidation the exchange current density was on the order of $250\mu\text{A}/\text{cm}^2$, while charge transfer coefficients were on the order of 0.05. For aging in chloride electrolyte, the exchange current density normalized to its original value, showed a trend of $-3.0 \pm 1.4 (\text{A}\cdot\text{h})^{-1}$ at the 95% confidence level. This slope was strongly affected by a few measurements yielding large values early on. Charge transfer coefficients were not found to change significantly. Control experiments, aging in electrolyte with no current delivered, showed a weak trend of $2.1\text{E-}4 \pm 1.2\text{E-}4 \text{ day}^{-1}$ for the reduction charge transfer coefficient, but the other parameters did not show trends. The exchange current density was lower in bromide electrolyte than chloride electrolyte, possibly due to the lower molar concentration compared with chloride electrolytes. The bromide exchange current densities were on the order of $50 \mu\text{A}/\text{cm}^2$, with charge transfer coefficients on the order of 0.03. For bromide electrolyte aging there were statistically significant trends in the aged oxidation charge transfer coefficient and the control exchange current density, of $-9.5 \times (10^{-3}) \pm 4.6 \times (10^{-3}) (\text{A}\cdot\text{h})^{-1}$ and $1.74 \times (10^{-5}) \pm 9.9 \times (10^{-6}) \text{ day}^{-1}$, respectively, at the 95% CL.

6.1 Future Work

Future work should continue with identification of the conditions necessary for protection of surfaces in greater detail. The parallel potentiostat flow cell experiment should be repeated with non-metallic voltage distribution and an AC power supply. The voltage profile field experiment could be ruggedized and re-attempted. Aging experiments would benefit from a refined routine to reduce the variability in measurements. These could also be conducted in a flow reactor with micro-electrodes, both to give a definite area, and because small electrodes behave better than large electrodes. The bromine aging tests were interrupted by reactor experiments, those tests could use more data points in the middle. The flow reactor experiments conducted could be re-designed with narrower channel gaps to increase product concentration.

Even though synthetic seawater is not all that different from chloride electrolyte, running mass spec on the product solution mixed with methyl methacrylate to determine which halogen species becomes attached would be very interesting and informative.

7. Bibliography

- [1] M. Delaney, "Study of Graphite-Polyurethane Composite Thin Film Electrodes for Their Use In Electrochemical Antifouling Systems," M.S., CBEE, Oregon State University, 2011.
- [2] P. Jacobson, G. Scott, and G. Hagerman, "Mapping and Assessment of the United States Ocean Wave Energy Resource," D. o. E.-E. P. R. Institute, Ed., ed, 2011.
- [3] S. McElvany. (2009, April 17). *Biofouling Prevention Coatings*. Available: <http://www.onr.navy.mil/Media-Center/Fact-Sheets/Biofouling-Prevention.aspx>
- [4] M. P. Schultz, "Effects of coating roughness and biofouling on ship resistance and powering," *Biofouling*, vol. 23, pp. 331-341, 2007.
- [5] J. Lewthwaite, A. Molland, and K. Thomas, "An Investigation into the Variation of Ship Skin Frictional Resistance with Fouling," *Transactions of the Royal Institute of Naval Architects* p. 15, 1984.
- [6] "Shipping, World Trade, and the Reduction of CO2 Emissions," International Chamber of Shipping, London 2014.
- [7] E. Almeida, T. C. Diamantino, and O. de Sousa, "Marine paints: The particular case of antifouling paints," *Progress in Organic Coatings*, vol. 59, pp. 2-20, 2007.
- [8] L. D. Chambers, K. R. Stokes, F. C. Walsh, and R. J. K. Wood, "Modern approaches to marine antifouling coatings," *Surface and Coatings Technology*, vol. 201, pp. 3642-3652, 2006.
- [9] M. Stupak, M. Garcia, and M. Perez, "Non-Toxic Alternative Compounds for Marine Antifouling Paints," *International Biodeterioration & Biodegradation*, vol. 52, pp. 49-52, 2003.
- [10] L. Adamson and N. Brown, "Focus on IMO: Anti-fouling systems," I. M. Organization, Ed., ed, 2003.
- [11] (7/28/2015). *Member States*.
- [12] (2012, 5/9/2013). *Australia confirms diuron bans and restrictions*. Available: <http://www.agra-net.com/portal2/ptcn/home.jsp?template=newsarticle&artid=20018008660&pubid=ag100>
- [13] "Washington SB 5436-2011-12," 2011 Regular Session ed, 2011.
- [14] M. Schütze, M. Malessa, V. Rohr, and T. Weber, "Development of coatings for protection in specific high temperature environments," *Surface and Coatings Technology*, vol. 201, pp. 3872-3879, 2006.
- [15] P. Bhadury and P. C. Wright, "Exploitation of marine algae: biogenic compounds for potential antifouling applications," *Planta*, vol. 219, pp. 561-578, 2004.
- [16] P.-Y. Qian, Y. Xu, and N. Fusetani, "Natural products as antifouling compounds: recent progress and future perspectives," *Biofouling*, vol. 26, pp. 223-234, 2009.
- [17] H. Lee, S. M. Dellatore, W. M. Miller, and P. B. Messersmith, "Mussel-Inspired Surface Chemistry for Multifunctional Coatings," *Science*, vol. 318, pp. 426-430, 2007.
- [18] T. Vladkova, "Surface Modification Approach to Control Biofouling," in *Marine and Industrial Biofouling*. vol. 4, H.-C. Flemming, P. S. Murthy, R. Venkatesan, and K. Cooksey, Eds., ed: Springer Berlin Heidelberg, 2009, pp. 135-163.
- [19] A. V. Bers and M. Wahl, "The Influence of Natural Surface Microtopographies on Fouling," *Biofouling*, vol. 20, pp. 43-51, 2004.
- [20] A. J. Scardino and R. de Nys, "Mini review: Biomimetic models and bioinspired surfaces for fouling control," *Biofouling*, vol. 27, pp. 73-86, 2010.

- [21] E. Pinori, M. Berglin, L. M. Brive, M. Hulander, M. Dahlstroem, and H. Elwing, "Multi-seasonal barnacle (*Balanus improvisus*) protection achieved by trace amounts of a macrocyclic lactone (ivermectin) included in rosin-based coatings," *Biofouling*, vol. 27, pp. 941-953, 2011.
- [22] G. Swain, A. C. Anil, R. E. Baier, F. S. Chia, E. Conte, A. Cook, *et al.*, "Biofouling and barnacle adhesion data for fouling-release coatings subjected to static immersion at seven marine sites," *Biofouling*, vol. 16, 2000.
- [23] C. J. Kavanagh, G. W. Swain, B. S. Kovach, J. Stein, C. Darkangelo-Wood, K. Truby, *et al.*, "The effects of silicone fluid additives and silicone elastomer matrices on barnacle adhesion strength," *Biofouling*, vol. 19, Dec 2003.
- [24] J. Stein, K. Truby, C. D. Wood, M. Takemori, M. Vallance, G. Swain, *et al.*, "Structure-property relationships of silicone biofouling-release coatings: Effect of silicone network architecture on pseudobarnacle attachment strengths," *Biofouling*, vol. 19, 2003.
- [25] Y. J. Sun, S. L. Guo, G. C. Walker, C. J. Kavanagh, and G. W. Swain, "Surface elastic modulus of barnacle adhesive and release characteristics from silicone surfaces," *Biofouling*, vol. 20, 2004.
- [26] E. R. Holm, C. J. Kavanagh, A. E. Meyer, D. Wiebe, B. T. Nedved, D. Wendt, *et al.*, "Interspecific variation in patterns of adhesion of marine fouling to silicone surfaces," *Biofouling*, vol. 22, 2006.
- [27] T. Matsunaga, T. Nakayama, H. Wake, M. Takahashi, M. Okochi, and N. Nakamura, "Prevention of marine biofouling using a conductive paint electrode," *Biotechnol. Bioeng.*, vol. 59, pp. 374-378, 1998.
- [28] H. Wake, H. Takahashi, T. Takimoto, H. Takayanagi, K. Ozawa, H. Kadoi, *et al.*, "Development of an electrochemical antifouling system for seawater cooling pipelines of power plants using titanium," *Biotechnol. Bioeng.*, vol. 95, pp. 468-473, 2006.
- [29] D. Mohn, M. Zehnder, W. J. Stark, and T. Imfeld, "Electrochemical disinfection of dental implants - a proof of concept," *PLoS One*, vol. 6, p. e16157, 2011.
- [30] P. Atkins, T. Overton, J. Rourke, M. Weller, and F. Armstrong, *Shriver & Atkins Inorganic Chemistry*: W. H. Freeman and Company, 2006.
- [31] T. Nakayama, H. Wake, K. Ozawa, N. Nakamura, and T. Matsunaga, "Electrochemical prevention of marine biofouling on a novel titanium-nitride-coated plate formed by radio-frequency arc spraying," *Appl. Microbiol. Biotechnol.*, vol. 50, pp. 502-508, 1998.
- [32] M. I. Kerwick, S. M. Reddy, A. H. L. Chamberlain, and D. M. Holt, "Electrochemical disinfection, an environmentally acceptable method of drinking water disinfection?," *Electrochim. Acta*, vol. 50, pp. 5270-5277, 2005.
- [33] T. Matsunaga, M. Okochi, M. Takahashi, T. Nakayama, H. Wake, and N. Nakamura, "TiN electrode reactor for disinfection of drinking water," *Water Res.*, vol. 34, pp. 3117-3122, 2000.
- [34] T.-K. Lim, T. Murakami, M. Tsuboi, K. Yamashita, and T. Matsunaga, "Preparation of a colored conductive paint electrode for electrochemical inactivation of bacteria," *Biotechnol. Bioeng.*, vol. 81, pp. 299-304, 2003.
- [35] M. Okochi, N. Nakamura, and T. Matsunaga, "Electrochemical killing of *Vibrio alginolyticus* using ferrocene-modified electrode," *Electrochim. Acta*, vol. 45, pp. 2917-2921, 2000.
- [36] A. von Jouanne, T. Lettenmaier, E. Amon, S. Moran, M. Bunn, and A. Yokochi, "Wave Energy Testing Using the Ocean Sentinel Instrumentation Buoy Including Testing of

- Materials and Technologies for Biofouling Resistant Surfaces," *Shore & Beach*, vol. 81, p. 8, 2013.
- [37] (2013). *Electric Power Annual 2013*. Available: <http://www.eia.gov/electricity/annual/pdf/epa.pdf>
- [38] *Advances in marine antifouling coatings and technologies*. Boca Raton, FL: CRC Press LLC, 2009.
- [39] J. J. Caprari, J. F. Meda, M. P. Damia, and O. Slutzky, "A Mathematical Model for Leaching in Insoluble Matrix Films," *Ind. Eng. Chem. Res.*, vol. 29, pp. 2129-2133, 1990.
- [40] D. M. Yebra, S. Kiil, K. Dam-Johansen, and C. E. Weinell, "Mathematical modeling of tin-free chemically-active antifouling paint behavior," *AIChE J.*, vol. 52, pp. 1926-1940, 2006.
- [41] "Product Data Sheet Hemptasil X3," Hempel, Ed., ed, 2014.
- [42] D. M. Yebra, S. Kiil, K. Dam-Johansen, and C. Weinell, "Reaction rate estimation of controlled-release antifouling paint binders: Rosin-based systems," *Progress in Organic Coatings*, vol. 53, Aug 1 2005.
- [43] S. Kiil, K. Dam-Johansen, C. E. Weinell, M. S. Pedersen, and S. A. Codolar, "Estimation of polishing and leaching behaviour of antifouling paints using mathematical modelling: a literature review," *Biofouling*, vol. 19, Apr 2003.
- [44] S. Kiil, C. E. Weinell, M. S. Pedersen, and K. Dam-Johansen, "Analysis of Self-Polishing Antifouling Paints Using Rotary Experiments and Mathematical Modeling," *Ind. Eng. Chem. Res.*, vol. 40, pp. 3906-3920, 2001.
- [45] J. A. Lewis, "Non-silicone biocide-free antifouling solutions," 2009, pp. 709-724.
- [46] R. E. Perez-Roa, M. A. Anderson, D. Rittschof, C. G. Hunt, and D. R. Noguera, "Involvement of reactive oxygen species in the electrochemical inhibition of barnacle (*Amphibalanus amphitrite*) settlement," *Biofouling*, vol. 25, pp. 563-71, 2009.
- [47] R. Krone and M. Paster, "Electrochemical antifouling system for structures wetted by seawater," EP2316584A1, 2011.
- [48] M. Legg, M. K. Yücel, I. Garcia de Carellan, V. Kappatos, C. Selcuk, and T. H. Gan, "Acoustic methods for biofouling control: A review," *Ocean Engineering*, vol. 103, pp. 237-247, 2015.
- [49] T. Harder and L. H. Yee, "Bacterial adhesion and marine fouling," 2009, pp. 113-131.
- [50] Y. Wang, J. Finlay, D. Betts, T. Merkel, C. Luft, M. Callow, *et al.*, "Amphiphilic Co-networks with Moisture-Induced Surface Segregation for High-Performance Nonfouling Coatings," *Langmuir*, vol. 27, p. 4, 2011.
- [51] S. Krishnan, C. J. Weinman, and C. K. Ober, "Advances in polymers for anti-biofouling surfaces," *Journal of Materials Chemistry*, vol. 18, pp. 3405-3413, 2008.
- [52] M. Salta, J. Wharton, P. Stoodley, S. Dennington, L. Goodes, S. Werwinski, *et al.*, "Designing biomimetic antifouling surfaces," *Philosophical transactions. Series A, Mathematical, physical, and engineering sciences*, vol. 368, pp. 4729-4754, 2010.
- [53] T. Matsunaga and T.-K. Lim, "Electrochemical prevention of biofouling," *Electrochemistry (Tokyo)*, vol. 68, pp. 847-852, 2000.
- [54] G. Liu, H. Wang, and H. Wang, "A pulse current method for propeller antifouling [Machine Translation]," CN103088345A, 2013.
- [55] H. Takayanagi, K. Ozawa, H. Kadoi, S. Osawa, and H. Waki, "Method for electrochemical control of fouling of structures contacting water," JP2008062187A, 2008.
- [56] S. Venkatesh and B. V. Tilak, "Chlor-alkali technology," *J. Chem. Educ.*, vol. 60, pp. 276-8, 1983.

- [57] J. A. Harrison, D. L. Caldwell, and R. E. White, "Electrocatalysis and the Chlorine Evolution Reaction," *Electrochimica Acta*, vol. 28, pp. 1561-1568, 1983.
- [58] S. Lower. (June 11). *Electrochemistry 4: The Nernst Equation*. Available: http://chemwiki.ucdavis.edu/Analytical_Chemistry/Electrochemistry/Electrochemistry_4%3A_The_Nernst_Equation
- [59] D. Pletcher and F. C. Walsh, *Industrial Electrochemistry*, 2 ed. New York, NY: Chapman and Hall, 1990.
- [60] A. International, "ASTM Standard G5, Standard Reference Test Method for Making Potentiodynamic Anodic Polarization Measurements," ed. West Conshohocken, PA: ASTM International, 2014.
- [61] X. L. Zhang, Z. H. Jiang, Z. P. Yao, Y. Song, and Z. D. Wu, "Effects of Scan Rate on the Potentiodynamic Polarization Curve Obtained to Determine the Tafel Slopes and Corrosion Current Density," *Corrosion Science*, vol. 51, pp. 581-587, 2009.
- [62] J. Newman and K. Thomas-Alyea, *Electrochemical Systems*, 3 ed. Hoboken, NJ: John Wiley & Sons, Inc, 2004
- [63] E. Eroğlu, S. Yapici, and O. N. Şara, "Some Transport Properties of Potassium Ferri/Ferrocyanide Solutions in a Wide Range of Schmidt Numbers," *Journal of Chemical & Engineering Data*, vol. 56, pp. 3312-3317, 2011.
- [64] A. J. Bard and L. R. Faulkner, *Electrochemical Methods*, 2 ed. Hoboken, NJ: John Wiley & Sons, Inc, 2001.
- [65] J. M. Commenge, L. Falk, J. P. Corriou, and M. Matlosz, "Optimal design for flow uniformity in microchannel reactors," *AIChE Journal*, vol. 48, pp. 345-358, 2002.
- [66] G. R. Ruschau, S. Yoshikawa, and R. E. Newnham, "Resistivities of Conductive Composites," *Journal of Applied Physics*, vol. 72, pp. 953-959, 1992.
- [67] D. Schroder, *Semiconductor Material and Device Characterization*: Wiley-IEEE Press, 2006.
- [68] K. S. Mohandas, N. Sanil, M. Noel, and P. Rodriguez, "Anodic behaviour of carbon materials in NaCl saturated NaAlCl₄ fused electrolyte at low temperatures: a cyclic voltammetric study," *J. Appl. Electrochem.*, vol. 31, pp. 997-1007, 2001.
- [69] O. V. Cherstiouk, P. A. Simonov, V. B. Fenelonov, and E. R. Savinova, "Influence of Nafion® ionomer on carbon corrosion," *Journal of Applied Electrochemistry*, vol. 40, pp. 1933-1939, 2010.
- [70] A. Bistrika, "Degradation of Graphite Electrodes in Acidic Bromine Electrolytes," Doctor of Philosophy, Chemical, Biological, and Environmental Engineering, Oregon State University, 2013.
- [71] O. Lanzi and U. Landau, "Terminal Effect at a Resistive Electrode under Tafel Kinetics," *Journal of the Electrochemical Society*, vol. 137, p. 4, 1990.
- [72] S. Marshall and S. Wolff, "Analysis of Terminal Effects in Rectangular Electrochemical Cells," *Electrochimica Acta*, vol. 43, p. 10, 1997.
- [73] H. S. Wroblowa, R. H. Hammerle, and R. L. Gealer, "Potential and Current Distributions Along Resistive Electrodes," *Journal of Applied Electrochemistry*, vol. 18, p. 3, 1988.
- [74] C. Zoski, *Handbook of Electrochemistry*: Elsevier, 2007.
- [75] A. Kerr, M. J. Cowling, C. M. Beveridge, M. J. Smith, A. C. S. Parr, R. M. Head, *et al.*, "The Early Stages of Marine Biofouling and its Effect on Two Types of Optical Sensors," *Environment International*, vol. 24, pp. 331-343, 1998.

- [76] D. Alsmeyer and R. McCreery, "In Situ Raman Monitoring of Electrochemical Graphite Intercalation and Lattice Damage in Mild Aqueous Acids," *Analytical Chemistry*, vol. 64, pp. 1528-1533, 1992.
- [77] T. Szabó, E. Tombácz, E. Illés, and I. Dékány, "Enhanced acidity and pH-dependent surface charge characterization of successively oxidized graphite oxides," *Carbon*, vol. 44, pp. 537-545, 2006.

Appendices

Appendix A.

Butler-Volmer Fitting Routine

```

%% Tafel parameter fitting routine
% Prepared by Malachi Bunn
% (c) 2015
% The script reads from an open EXCEL file with the name identified at
% line 20.
% Output parameters are given in table "params"
% Data should be taken in linear form (not logarithmic axis view which
% gives absolute value for NPV or log values for Tafel experiments)
% Script Expects voltages in the first column, with currents in the
second
% column. The script automatically reads every other column to
minimize
% post-processing demands when copying data from the Gamry E-chem
analyst
% software. Results are written to Sheet 2 of the source workbook.

%% Initialize
clear all
format compact
clc

%% IDENTIFY DATA FILE
filename = '20150805 MB03_71D.xlsx';
%% Constants, initial guesses

R = 8.314; %J/mol-K
T = 298; %K
n = 2;
F = 96485; %C/mol
E0 = ones(1,18);
E0 = 1.2*E0; % initial guess, OCP, to avoid issues with shifting let it
float
aox = ones(1,18); %create a vector of charge transfer coefficient
values
aox = aox*0.5; %initial guess, oxidation charge transfer coefficient
ared = aox; %initial guess, reduction charge transfer coefficient
i0 = ones(1,18); %create a vector of exchange current density values
i0 = i0*10^-5; %mA/cm^2, initial guess of exchange current density
j = 1; %counter
i = 1; %counter
nrows = 41; %will verify, but rows expected in data
ncolumns = 18; %will verify, but columns expected in data

%% Data input

%Load data from file
[tbl, alltxt] = xlsread(filename, 'Sheet1'); %read all data

%Check size of dataset
[nrows, ncolumns] = size(tbl);

```

```

%ncolumns/2 sets of data
ncolumns = ncolumns/2;
data = zeros(nrows,ncolumns);
V = zeros(nrows,ncolumns);
for j = 1:ncolumns;
    %Load current data, in Amps
    data(:,j)= tbl(:,2*j);
    %Load Voltage data, in V is vs Ag|AgCl in 1M KCl
    V(:,j) = tbl(:,((2*j)-1));
    j=j+1;
end

%% Model definition
b = [0.5, 0.5, 0.8, 10^-4]; %parameter matrix
BVmodel = @(b,V) b(4)*(exp(n*F/R/T*b(1)*(V-b(3)))-
exp(n*F/R/T*b(2)*(b(3)-V))); %Butler Volmer model

%% Model Fitting
opts = statset('TolFun',1e-10, 'MaxIter', 1e4); %'Display','iter', to
display iterations
paramnames = {'aox'; 'ared'; 'E0'; 'i0'};
params = table('RowNames', paramnames);
names = table('RowNames',{'Experiment Name'});
for j=1:ncolumns;
    %Read column names
    names(1,j) = alltxt(2,j*2);

    %Fit the model
    mdl = fitnlm(V(:,j),data(:,j),BVmodel,[0.02, 0.02, 0.8, 10^-
2], 'Options', opts);

    %Store solved parameter values
    for i=1:4;
        params(i,j) = mdl.Coefficients(i,1);
    end

    j=j+1;
end

%Pass results back to source workbook
xlswrite(filename,paramnames, 'Sheet2', 'A2:A5');
namesx = table2cell(names);
xlswrite(filename,namesx, 'Sheet2', 'B1');
paramsx = table2array(params);
xlswrite(filename, paramsx, 'Sheet2', 'B2');

```

Appendix B.

Constants Used in Model Parameter Fitting

Name	Symbol	Value	Units	
Chloride Diffusivity	D_{Cl^-}	2.03E-9	m ² /s	Atkins Pchem
Chlorine Diffusivity	D_{Cl_2}	1.25E-9	m ² /s	Cussler
Hypochlorite Charge Transfer Coefficient	α	0.04		
Hypochlorite Exchange Current	i_0	0.45	A/m ²	
Hypochlorite Inlet Concentration	D_{HClO}	10 ⁻¹²	M	
Chloride Inlet Concentration	D_{Cl}	0.6	M	
Viscosity of Water	μ_{H_2O}	0.001	Pa-s	
Temperature	T	298	K	
Gas Constant	R	8.314	J/mol-K	
Density of Water	ρ	1020	kg/m ³	

